

1. Report No. FHWA/TX-92+1195-1	2. Government Accession No.	3. Recipient's Catalog No.	
4. Title and Subtitle NUMERICAL MODELING OF THE RESPONSE OF CYLINDRICAL SPECIMENS OF CLAY TO DRYING		5. Report Date November 1991	6. Performing Organization Code
7. Author(s) Douglas O'Neal Bell and Stephen G. Wright		8. Performing Organization Report No. Research Report 1195-1	
9. Performing Organization Name and Address Center for Transportation Research The University of Texas at Austin Austin, Texas 78712-1075		10. Work Unit No. (TRAIS)	11. Contract or Grant No. Research Study 3-8-89/1-1195
12. Sponsoring Agency Name and Address Texas Department of Transportation Transportation Planning Division P. O. Box 5051 Austin, Texas 78763-5051		13. Type of Report and Period Covered	
15. Supplementary Notes Study conducted in cooperation with the U. S. Department of Transportation, Federal Highway Administration. Research Study Title: "Long-Term Strength Properties of Compacted Fills for Embankment Design"		14. Sponsoring Agency Code	
16. Abstract Previous research has indicated that the rate at which soil dries influences the incidence and severity of cracking in soil. Cracking of soil is caused by tensile stresses created by unequal shrinkage strains that develop because the soil surface dries more quickly than the interior of the soil. A theoretical model of drying cylindrical specimens of clay was developed based on Biot's general theory of three-dimensional consolidation. A numerical model of drying was developed by employing the finite element method to solve the coupled equation governing equilibrium and flow derived in the theoretical model. A parametric study of consolidation of cylindrical specimens of clay was performed to validate the numerical model. Another parametric study was then performed to investigate the effect of different rates of drying on the development of tensile stress in cylindrical specimens of clay.			
17. Key Words numerical modeling, response, clay, drying, cylindrical, specimens, soil, cracking, tensile stresses, shrinkage strains, equilibrium, flow, surface, interior, parametric study		18. Distribution Statement No restrictions. This document is available to the public through the National Technical Information Service, Springfield, Virginia 22161.	
19. Security Classif. (of this report) Unclassified	20. Security Classif. (of this page) Unclassified	21. No. of Pages 48	22. Price

NUMERICAL MODELING OF THE RESPONSE OF CYLINDRICAL SPECIMENS OF CLAY TO DRYING

by

Douglas O'Neal Bell
Stephen G. Wright

Research Report Number 1195-1

Research Project 3-8-89/1-1195
Long-Term Strength Properties of Compacted Fills for Embankment Design

conducted for

Texas Department of Transportation

in cooperation with the

**U.S. Department of Transportation
Federal Highway Administration**

by the

**CENTER FOR TRANSPORTATION RESEARCH
Bureau of Engineering Research
THE UNIVERSITY OF TEXAS AT AUSTIN**

November 1991

NOT INTENDED FOR CONSTRUCTION,
PERMIT, OR BIDDING PURPOSES

Stephen G. Wright (Texas No. 49007)
Research Supervisor

The contents of this report reflect the views of the authors, who are responsible for the facts and the accuracy of the data presented herein. The contents do not necessarily reflect the official views or policies of the Federal Highway Administration or the Texas Department of Transportation. This report does not constitute a standard, specification, or regulation.

PREFACE

Project 1195 was undertaken to develop procedures for determining the long-term strength properties of compacted clay fills for embankment design. Particular attention was focused on the effects that wetting and drying had on the shear strength properties of high plasticity clays. As part of the investigation, specimens were compacted in the laboratory and subjected to repeated cycles of wetting and drying in an effort to approximate effects in the field and to reproduce the cracking that had been observed in the field. Preliminary studies revealed that the rate of drying had a significant effect on the formation of cracks in laboratory specimens. Accordingly, a literature review and theoretical study were undertaken to better understand the effects of drying rate and to determine important parameters that affected the formation of cracks. This report contains the results of the literature review and theoretical studies, including the development of a simple numerical model that was used to study the effects of drying rate on the development of tensile stresses and, thus, cracking in specimens that were dried.

LIST OF REPORTS

Research Report No. 1195-1, "Numerical Modeling of the Response of Cylindrical Specimens of Clay to Drying," by Douglas O'Neal Bell and Stephen G. Wright, presents the results of the literature review and theoretical studies, including the development of a simple numerical model that was used to study the effects of drying rate on the development of tensile stresses and, thus, cracking in specimens that were dried. November 1991.

Research Report No. 1195-2F, "Investigation of Long-Term Strength Properties of Paris and Beaumont Clays in Earth Embankments," by Mohamad K. Kayyal and Stephen G. Wright, presents the results of laboratory studies on the shear strength properties and comparisons of the results from the laboratory tests with observed field behavior of embankments which have failed. November 1991.

ABSTRACT

Previous research has indicated that the rate at which soil dries influences the incidence and severity of cracking in soil. Cracking of soil is caused by tensile stresses created by unequal shrinkage strains that develop because the soil surface dries more quickly than the interior of the soil. A theoretical model of drying cylindrical specimens of clay was developed based on Biot's general theory of three-dimensional consolidation. A numerical model of drying was developed by employing the finite element method to solve the coupled equation governing equilibrium and flow derived in the theoretical model. A parametric study of consolidation of cylindrical specimens of clay was performed to validate the numerical model. Another parametric study was then performed to investigate the effect of different rates of drying on the development of tensile stress in cylindrical specimens of clay.

SUMMARY

A numerical model was developed and implemented to predict the process of drying and the development of tensile stresses in cylindrical specimens. The numerical model is based on Biot's general theory of three-dimensional consolidation and is solved employing the finite element method. Parametric studies were performed with the numerical model to examine how drying rate and soil properties might influence the formation of cracks. The theoretical studies confirmed that different rates of drying will influence the magnitude of tensile stresses and, thus, will influence the cracking expected in specimens. The numerical model is believed to provide a useful tool for studying cracking in soil specimens and is an important first step in modeling the behavior.

IMPLEMENTATION STATEMENT

The principal purpose of that portion of Research Study 1195 addressed in this report was to provide a basic theoretical framework for guiding other laboratory tests and interpreting the results of those tests. The model is believed to be particularly useful for researchers studying the effects of cracking produced by drying. Although the theoretical model is not intended to be a model for routine laboratory analysis or design, the researchers believe that it is important to document the model and to make it available to other researchers involved with similar studies.

ACKNOWLEDGMENTS

The authors are grateful to Dr. José Roesset for his assistance in developing the finite element model upon which this research is based.

The authors are also grateful for the help of David Lutz, Paula Estornell, Kathy Darr, Bob Gauer, Mihalis Madianos, and Gerald Eykholt, who are graduate students at The University of Texas at Austin.

Finally, the support of the Texas Department of Transportation for this research is gratefully acknowledged.

TABLE OF CONTENTS

PREFACE	iii
LIST OF REPORTS	iii
ABSTRACT	iii
SUMMARY	iv
IMPLEMENTATION STATEMENT	iv
ACKNOWLEDGMENTS	iv
CHAPTER 1. INTRODUCTION	1
CHAPTER 2. RESPONSE OF SOILS DURING DRYING	
2.1 INTRODUCTION	2
2.2 EVAPORATION FROM SOIL	2
2.2.1 <i>Turbulent Mass Transfer Coefficient</i>	2
2.2.2 <i>Concentration Difference</i>	3
2.3 STAGES OF DRYING	3
2.3.1 <i>Constant Rate Stage</i>	4
2.3.2 <i>Falling Rate Stage</i>	5
2.4 INCONSISTENCIES	5
2.5 DRYING STRESSES	6
2.6 SUMMARY	6
CHAPTER 3. GOVERNING PARTIAL DIFFERENTIAL EQUATIONS	
3.1 INTRODUCTION	7
3.2 ASSUMPTIONS	7
3.3 EQUILIBRIUM EQUATION	7
3.4 FLOW EQUATION	9
3.5 SUMMARY	10
CHAPTER 4. FINITE ELEMENT FORMULATION	
4.1 INTRODUCTION	11
4.2 DISCRETIZATION	11
4.3 PRINCIPLE OF VIRTUAL WORK	11
4.3.1 <i>Equilibrium Equation</i>	12
4.3.2 <i>Flow Equation</i>	13
4.4 SOLUTION PROCEDURE	13
4.5 BOUNDARY CONDITIONS	14
4.6 COMPUTATION OF STRESSES	16
4.7 SUMMARY	16

CHAPTER 5. VERIFICATION OF THEORETICAL MODEL AND COMPUTER PROGRAM	
5.1 INTRODUCTION	17
5.2 DEGREE OF CONSOLIDATION AND AVERAGE PORE WATER PRESSURE	17
5.3 MODELING EFFECTS	17
5.4 TERZAGHI'S SOLUTION FOR CONSOLIDATION	18
5.5 INPUT PARAMETERS	19
5.6 EVALUATING THE MODEL	20
5.7 THE MANDEL-CRYER EFFECT	21
5.8 SUMMARY	22
CHAPTER 6. NUMERICAL RESULTS OF DRYING SIMULATIONS	23
6.1 INTRODUCTION	23
6.2 MODELING EFFECTS	23
6.2.1 <i>Number of Elements</i>	23
6.2.2 <i>Time Step</i>	23
6.3 SPECIMEN CHARACTERISTICS AND RATES OF DRYING	23
6.4 TYPICAL RESULTS	25
6.5 INTERPRETATION OF RESULTS	26
6.6 EFFECT OF RATE OF DRYING	27
6.7 EFFECT OF POISSON'S RATIO	30
6.8 SUMMARY	31
CHAPTER 7. SUMMARY, CONCLUSIONS, AND RECOMMENDATIONS	
7.1 SUMMARY	32
7.2 CONCLUSIONS	32
7.3 RECOMMENDATIONS	33
APPENDIX A	
A.1 INTRODUCTION	35
A.2 EQUILIBRIUM EQUATION	35
A.3 FLOW EQUATION	38
A.4 SUMMARY	39
BIBLIOGRAPHY	41

CHAPTER 1. INTRODUCTION

In the past decade, a number of highway embankments in the Houston area have experienced shallow slides of 3 to 5 feet in depth. Typically the embankments are less than 30 feet high and have side slopes ranging from approximately 2:1 to 3:1 (horizontal:vertical). The embankments were constructed of highly plastic clays and have been in service from 10 to 30 years. Studies were conducted to evaluate the shear strength of the embankment material (Gourlay and Wright, 1984; Stauffer and Wright, 1984), and it was discovered that shear strengths at failure are significantly lower than laboratory data suggest. It was thought that repeated cycles of wetting and drying and the associated cracking of the soil might be responsible for the reduced shear strength. The effects of wetting and drying were studied by Kayyal (1986). His studies indicated that the severity of cracking experienced in laboratory specimens was directly related to the rate at which the specimens were dried.

The present study was initiated to investigate the effect of the rate of drying on the development of cracks in laboratory specimens. The objective of the study was to develop a numerical model to simulate drying of specimens. During drying, the effective stress in the specimens increases as pore water evaporates, and the pore water pressures become increasingly negative. As the effective stresses increase, the specimens shrink (decrease in volume); therefore, the drying process is similar to the process of consolidation.

The numerical model employs the finite element method to solve the coupled equations of equilibrium and flow established by Biot in his general theory of three-dimensional consolidation (Biot, 1941). The model assumes a fully saturated soil, which seems reasonable for the intended application because experiments indicate that almost all shrinkage of the specimens occurs while the

soil is saturated. A linearly elastic, homogeneous soil is assumed for simplicity. It is assumed that either the surface pore water pressure or the flux of water across the surface boundary is known and that evaporation occurs under isothermal conditions.

A FORTRAN computer program, SHRINK, was written to implement the numerical model. To verify the model and the computer program, the dissipation of excess pore water pressure in a specimen during consolidation was computed and compared with values computed using Terzaghi's theory of one-dimensional consolidation. Additional computations were performed using soil properties selected to represent laboratory specimens of Taylor Marl studied by Kayyal (1986) and Cuenca (1989). These computations were used to evaluate the effect of different rates of drying on the development of tensile stress in specimens.

The process of evaporation and the response of soil to drying is discussed in Chapter 2. The derivation of the governing differential equations that describe the drying and shrinkage of cylindrical specimens is given in Chapter 3. Chapter 4 presents the development of the numerical model, which is based on a finite element formulation of the equations derived in Chapter 3. In Chapter 5, the validity of the numerical model is examined in the context of consolidation of soil. The effects of the rate of drying and of Poisson's ratio on the development of tensile stress in cylindrical specimens are evaluated in Chapter 6. Typical results obtained from the numerical model are also presented in this chapter. Conclusions and recommendations are presented in Chapter 7. Detailed derivation of the component matrices, which are combined to form the stiffness matrices used in the finite element model, is presented in an Appendix.

CHAPTER 2. RESPONSE OF SOILS DURING DRYING

2.1 INTRODUCTION

Drying of soil consists of removal of pore water by evaporation. Drying is most commonly accomplished by adding heat to the soil to increase the evaporative potential. As pore water is removed, the pore water pressure in the soil decreases (becomes more negative), which increases the effective stress on the soil. The increase in effective stress causes the soil to shrink. A non-uniform increase in effective stress in the soil will create differential strains which can cause cracking. Experiments have shown that the rate of drying, the drying conditions, and the initial conditions of the soil affect its behavior during drying.

2.2 EVAPORATION FROM SOIL

The evaporation of water from soil is a complex thermodynamic process involving the transfer of heat and mass across a finite boundary. The rate of evaporation from soils depends upon the atmospheric conditions of air temperature, air pressure, and air velocity. It also depends upon the soil properties which govern the transport of water through the soil. The rate of evaporation from soils is usually expressed as the mass flux of water vapor moving, in response to a concentration gradient, across a boundary air film into the region of turbulent mixing of the atmosphere. For a constant total water vapor concentration and constant rate of heat transfer, the rate of evaporation can be expressed mathematically as (Lebedev, 1961; Budyko, 1963; Geankoplis, 1983):

$$E = -(D_{w-a} + \epsilon_m(z)) \frac{\partial c}{\partial z} \quad 2.1$$

where

- E = evaporative flux of water vapor, kg/m² s;
- c = concentration of water vapor, kg/m³;
- z = coordinate in the direction of moisture movement normal to the evaporative surface, m;

- D_{w-a} = molecular diffusivity of water vapor through air, m²/s; and
- ϵ_m = mass eddy diffusivity, m²/s.

A more useful form of Equation 2.1 is obtained by assuming an average value for the mass eddy diffusivity, $\bar{\epsilon}_m$, over the boundary thickness, Δz , and integrating with respect to z to give (Geankoplis, 1983):

$$E = k'(c_s - c_a) \quad 2.2$$

in which

$$k' = \frac{(D_{w-a} + \bar{\epsilon}_m)}{\Delta z} \quad 2.3$$

and the subscripts "s" and "a" indicate values at the soil surface and in the atmosphere, respectively. The coefficient k' is called the turbulent mass transfer coefficient and has the units of length per unit time. Equation 2.2 provides a convenient basis for discussion of the factors which affect the rate of evaporation from soil. The effect of various factors can be examined in terms of their effect on the values of k' and $(c_s - c_a)$.

2.2.1 Turbulent Mass Transfer Coefficient

As shown in Equation 2.2, the turbulent mass transfer coefficient, k' , is determined by the values of the molecular diffusivity of water in air, the mass eddy diffusivity, and the boundary thickness. The molecular diffusivity, D_{w-a} , is constant for a given temperature and pressure; the value is 0.25×10^{-4} m²/s at 20°C and atmospheric pressure (Geankoplis, 1983). The average mass eddy diffusivity, $\bar{\epsilon}_m$, accounts for the movement of water vapor through the transitional zone of the boundary layer by eddy diffusion. The value of $\epsilon_m(z)$, in Equation 2.1, is close to zero near the surface of the soil and increases with increasing

distance from the surface. The exact variation is, in general, unknown; thus, the use of an average value is necessary. The thickness of the boundary layer is also not generally known. Thus, k' is usually determined experimentally (Geankoplis, 1983). According to boundary layer theory, the thickness of the boundary layer and the intensity of turbulence, which both affect $\bar{\epsilon}_m$, are related to the velocity of the air flow across the surface and the surface roughness of the soil. Increasing air velocity reduces the boundary layer thickness and, therefore, increases the rate of evaporation from soil. Increasing surface roughness creates greater turbulence within the boundary layer, which results in larger values of $\bar{\epsilon}_m$ and thereby increases the rate of evaporation from soil.

2.2.2 Concentration Difference

The difference between the concentration of water vapor in the atmosphere and at the soil surface, $c_s - c_a$, is affected by the conditions which determine the values of both concentrations. The water vapor concentration in the atmosphere, c_a , is primarily a function of the air temperature and pressure according to the Ideal Gas Law. It is also affected by the velocity of the air flow across the evaporative surface. Increasing air temperature and/or decreasing air pressure cause a decrease in the value of c_a . The water vapor concentration at the soil surface, c_s , is a unique function of the capillary pressure (suction pressure) of the soil according to the relation (Keey, 1972):

$$P_s = -\frac{RT}{\bar{V}_w} \ln\left(\frac{c_s}{c_{sat}}\right) \quad 2.4$$

where

- P_s = suction pressure of the soil, kPa;
- T = absolute temperature, °K;
- R = universal gas constant, 8.314 kJ/kmol-°K;
- \bar{V}_w = molal volume of liquid water, 0.018 m³/kmol;
- c_s = concentration of water vapor, kg/m³; and
- c_{sat} = saturated concentration of water vapor, kg/m³.

The molal volume of liquid water, \bar{V}_w , given in m³/kmol, is the volume which is occupied by 1 kmole (kilomole: = 1,000 • Avogadro's No. of units) of water molecules. The value of \bar{V}_w depends slightly on the temperature and pressure of the water, but in the range of temperature and pressure considered valid for drying soils, this

volume is effectively constant. According to Equation 2.4, for a given temperature, an increase in soil suction causes a decrease in water vapor concentration in the soil. For drying of clay soils, where the suction pressure increases significantly with the removal of pore water, the value of c_s must decrease rapidly. If the atmospheric conditions are constant (c_a constant), then a decrease in c_s due to drying reduces the difference between c_s and c_a and therefore reduces the rate of evaporation from soil.

2.3 STAGES OF DRYING

Based on previous research summarized by Hillel (1982) and Keey (1972), the process of drying under constant atmospheric conditions, i.e., constant temperature, pressure, air velocity and relative humidity, occurs in at least two distinct stages: (1) a constant rate of drying stage, and (2) a falling rate of drying stage. The rate of drying is usually expressed as the amount of water (either mass or volume) removed from the soil per unit area of drying surface per unit time (Hlavác, 1983). This rate is consistent with the evaporation rate, E , in Equation 2.1. The two stages of drying can be identified on a "drying rate curve," which is a curve showing the relationship between the rate of drying and the moisture content of the soil (Meiners, 1988). Typical drying rate curves for clay are shown in Figure 2.1.

The transition between the two stages of drying is generally sharp (Hillel, 1982). The moisture content at which this transition occurs is referred to as the "critical moisture content," ω_{cr} (Keey, 1972; Hall, 1979; Worrall, 1986; Meiners, 1988). Keey (1972) and Meiners (1988) indicate that the critical moisture content is due to a transition in the way moisture is retained by soil as it dries. They assert that ω_{cr} is the moisture content of the soil after all free water has been removed from the voids. (This implies that it represents the moisture content due only to absorbed water—so the soil must already be unsaturated by this point). Typical values of ω_{cr} for a variety of clays were summarized by Keey (1972) and are presented in Table 2.1. Hlavác (1983) notes that the transition between the two stages of drying is not always defined by an explicit critical moisture content but may be more gradual. Worrall (1986) reports that ω_{cr} depends upon the initial water content of the soil. Keey (1972) states that the initial drying rate affects the critical moisture content. Observations of soil behavior during the two stages of drying are presented in the next two sections.

2.3.1 Constant Rate Stage

When drying of a saturated clay begins at a high water content, the evaporative surface where water vapor is formed is located at the surface of the clay. For some period of time, which may be quite short, the surface water exists as a continuous film and drying occurs at a constant rate. Under constant external conditions the rate of drying during this constant rate stage is approximately equal to the rate of evaporation from a free water surface (Keey, 1972; Hlavác, 1983; Lawrence, 1972; Worrall, 1986). As water is removed from the pores of the specimen, the clay particles are drawn together by capillary stresses in the voids (Hlavác, 1983; Lawrence, 1972) and the specimen shrinks. The capillary stresses responsible for shrinkage while the soil remains saturated have been reported to range from 263 psi for kaolinite to 880 psi for ball clay (Lawrence, 1972). During the constant rate stage of drying, the reduction in volume of the clay due to shrinkage is equal to the volume of pore water removed (Lawrence, 1972; Johnston and Hill, 1944), which indicates that the clay remains saturated during the constant rate stage as long as it undergoes shrinkage. However, shrinkage may cease (and, thus, the soil may

become unsaturated) before the end of the constant rate stage is reached.

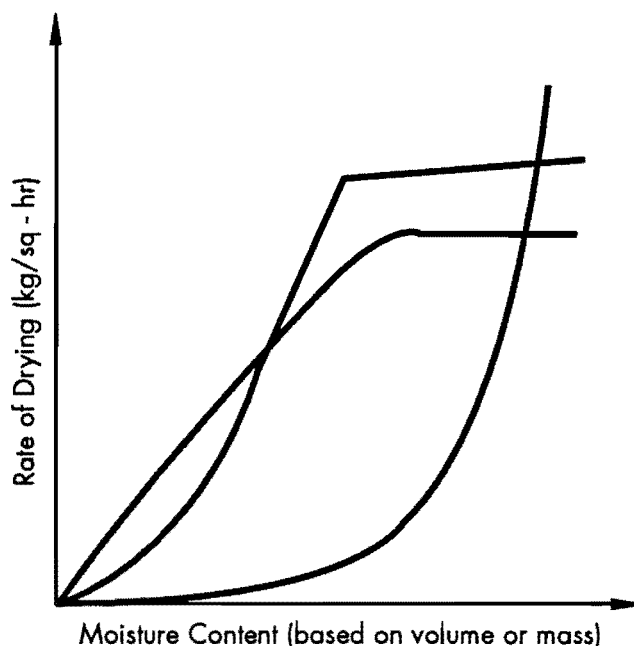


Figure 2.1 Typical drying rate curves for three different soils illustrating the two stage process of drying (after Keey, 1972; Hlavác, 1983)

Table 2.1 Approximate critical moisture contents for various soils (from Keey, 1972)

Soil	Air Velocity (m/s)	Air Temperature (°C)	Relative Humidity	Critical Moisture Content (kg/kg)
Common brick clay	1	37	0.10	0.11
Common brick clay	1	32	0.15	0.13
Common brick clay	10.6	25	0.40	0.17
Silica brick	3.4	55	0.12	0.093
Plastic mix	3.4	55	0.11	0.193
Flint mix	3.4	55	0.10	0.127
Kibushi	2.1	15	0.37	0.152
Kibushi	2.1	45	0.37	0.186
Kibushi	2.1	35	0.19	0.20
Kibushi	2.1	35	0.76	0.21
Kaolin/Feldspar	0.3	40	N/A	0.099
5:5	0.3	90	N/A	0.03
5:5	0.5	40	0.30	0.098
5:5	9.2	40	0.30	0.134
5:5	2.1	30	0.30	0.178
5:5	2.1	30	0.30	0.088
Kaolin/Feldspar	2.1	40	0.40	0.13
7.3				
Kaolin	2.1	40	0.40	0.181

2.3.2 Falling Rate Stage

The falling rate stage of drying is characterized by a continuous, but not necessarily steady, reduction in the rate of drying of the soil. According to Hillel (1982), the rate of drying during this stage is controlled by the conditions of moisture retention and moisture movement which limit the supply of water to the evaporative surface. Some researchers contend that the falling rate stage corresponds to a period of drying in which no volume change occurs in the soil (Worrall, 1986; Lawrence, 1972). This suggests that the degree of saturation of the clay must decrease because the volume of pore water removed by drying is replaced by air. This does not imply that the beginning of the falling rate stage coincides with the soil becoming unsaturated; the soil may have already become unsaturated before the critical moisture content was reached. As the degree of saturation decreases, the flow of liquid water through the soil is retarded by the presence of air in the voids, and the rate of flow of water to the evaporative surface begins to limit the rate of surface evaporation.

In some instances the location of the evaporative surface shifts from the soil surface to some level within the soil (Hlavác, 1983; Hillel, 1982; Lawrence, 1972). Hillel (1982) has called the evaporative surface a "drying front" when it exists below the soil surface, and Hall (1979) defines a drying front as a layer which separates dry material from moist material. The progress of a drying front below the soil surface implies that the water vapor which is formed there must diffuse through the overlying crust of dry soil before entering the atmosphere. Thus, the increased length of diffusion significantly reduces the rate of drying, as shown by Equation 2.1.

2.4 INCONSISTENCIES

There is some evidence to suggest that soil behavior during drying is inconsistent with some of the observations reported in Section 2.3. Clay shrinks as it dries, which requires that the effective stress in the soil increase. Since the total stress applied to the soil is essentially zero (atmospheric pressure), the increase in effective stress must be due to a decrease in pore water pressure. According to Equation 2.4, a reduction in pore water pressure causes a reduction in the rate evaporation from the soil, so the rate of drying of the soil must decrease. But many researchers report that all shrinkage of clays due to drying occurs during the constant rate stage of drying (Lawrence, 1972; Worrall, 1986). Keey (1972) states explicitly that

some research indicates that the critical moisture content in kaolinitic clays corresponds to the limit of shrinkage. He also reports that some drying experiments do not show a constant rate of drying stage. Hlavác (1983) has also observed that the rate of drying during the stage where shrinkage occurs is not constant.

A reasonable explanation for the inconsistent observations is suggested by Keey (1972) and also by Hlavác (1983). They remark that the effect of soil suction on the concentration of water vapor during the initial drying stage contributes to a non-constant rate of drying. Hlavác (1983) notes that the rate of drying is affected by a reduced vapor pressure (vapor concentration) due to negative curvature of the water level in the surface pores (negative pore water pressure). The effect of the soil suction on the rate of drying can be seen in Figure 2.2, in which the relationship between soil suction and relative water vapor concentration (relative humidity) given in Equation 2.4 is shown for a temperature of 300°K (27°C). For the typical range of soil suction of interest, from 0 psi to 2,000 psi (Olson, 1990), the relative humidity in the soil is nearly constant. Thus, as the soil dries and the soil suction increases, the rate of drying, according to Equation 2.2, must decrease. However, the change in the rate of drying is small enough that the rate of drying appears to be nearly constant.

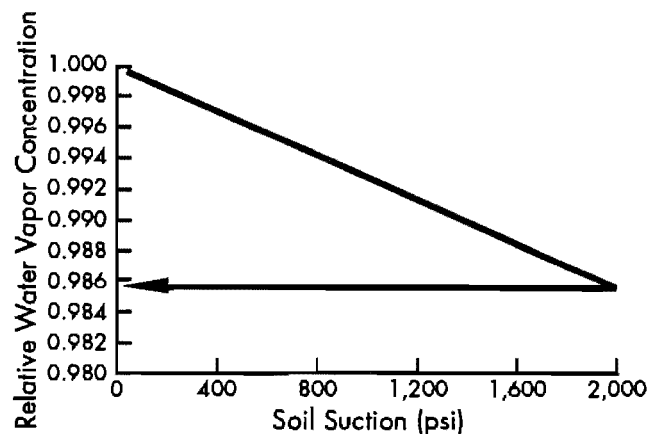


Figure 2.2 Variation of relative water vapor concentration (relative humidity) for the range of expected maximum soil suction (Eq 2.4 at 27°C and 1 atm)

Keey (1972) suggests that clay specimens require a warm-up period during which the process of heat transfer affects the drying rate. Initially, the drying rate is small, and it increases as the soil is heated. According to Keey, the increase in drying rate during the warming period may be offset by

decreases in the rate of drying due to decreasing pore water pressures. These effects may also tend to create the approximately constant rate of drying which has been observed.

2.5 DRYING STRESSES

Drying causes changes in the stresses in a soil which may cause the soil to crack. Cracking is caused by the development of tensile stress due to unequal drying strains (Phelps et al., 1982). The unequal strains are the result of incompatibility between the flow of moisture from the interior of the soil and the rate of evaporation at the soil surface. As the soil surface dries and shrinks, a pressure gradient is established between the high pore water suction at the surface and the lower pore water suction in the interior of the soil (Hillel, 1982). If the rate of evaporation at the surface is high, then the flow of water from the interior can not fully replenish the evaporated moisture and the soil surface begins to dry. As the surface zone of the soil dries, it shrinks onto the incompressible moist soil core (Keey, 1972). The differential shrinkage establishes tensile stresses in the dried zone which can cause cracking if the tensile stresses exceed the tensile strength of the soil (Keey, 1972; Worrall, 1986). This qualitative relationship between the rate of drying and the potential for cracking has

been observed by Lawrence (1972), Worrall (1986), Hlavác (1983), and Kayyal (1986).

2.6 SUMMARY

The drying of soil is a complex process which is affected by the factors controlling the rate of evaporation at the soil surface and the flow of pore water through the soil voids. Evaporation at the soil surface occurs by molecular diffusion of water vapor across a finite boundary layer. The rate of evaporation is determined by atmospheric variables and by the properties of the soil surface.

The drying of soil has been observed to occur in two distinct stages: (1) an initial stage in which the rate of drying is constant, and (2) a second stage in which the rate of drying decreases. The moisture content which marks the transition between the two stages is termed the "critical moisture content," ω_{cr} .

Shrinkage of soil occurs almost entirely during the constant rate stage of drying. Shrinkage occurs while the soil remains nearly saturated such that the volume of shrinkage is equal to the volume of water removed from the soil.

The rate of drying influences the state of stress in the drying soil. Evidence suggests that rapid drying rates create tensile stresses near the soil surface which can cause the surface to crack.

CHAPTER 3. GOVERNING PARTIAL DIFFERENTIAL EQUATIONS

3.1 INTRODUCTION

As soil dries, the state of stress in the soil changes. The state of stress changes because the pore water pressure changes as water is removed. The soil changes in volume (shrinks) in response to the changing state of stress during drying; when the change in stress is severe, the soil may crack.

A theoretical model of drying and shrinkage of laboratory specimens was developed to provide insight into the initiation of cracking in specimens subjected to drying. It was hoped that the theoretical model could demonstrate that the rate of drying of a soil specimen significantly affects the development of tension, and thus cracking, in the soil as it dries.

The theoretical model is presented in this chapter. The model is based on the equations for consolidation of soil presented by Biot (1941) in his general theory of three-dimensional consolidation.

3.2 ASSUMPTIONS

Several assumptions were made concerning the properties of the soil and pore water. These are:

1. The soil skeleton is a linearly elastic, isotropic material, characterized by two elastic constants: Young's modulus (E) and Poisson's ratio (ν). The elastic constants are used to relate strains to effective stresses using Hooke's Law.
2. The soil is saturated and remains saturated during moisture removal.
3. Water is incompressible.
4. Water flows according to Darcy's law.
5. Terzaghi's principle of effective stress is valid.

These assumptions are essentially the same as those used in Terzaghi's theory of one-dimensional consolidation. The only significant difference is that the present solution relates the complete state of stress in the soil to the two- and three-

dimensional state of deformation using two elastic constants, E and ν , while Terzaghi related the state of stress to the deformation through a single "elastic" constant, m_v , the coefficient of volume change.

The theoretical model was developed to simulate the drying of a typical cylindrical specimen of clay of the type used in triaxial shear tests. Accordingly, the following assumptions were made concerning the specimen geometry and the deformation during drying:

1. The specimen is a right circular cylinder of constant cross section.
2. The deformation is plane strain, i.e., the strain in the axial direction is zero, $\epsilon_z = 0$.
3. There are no stresses applied to the surface of the specimen; body forces and inertia forces are neglected.

These assumptions are used in the following two sections to develop the equations governing force equilibrium and flow in the specimen, which constitute the theoretical model of drying.

3.3 EQUILIBRIUM EQUATION

The equilibrium equations for an elemental volume of soil, like the one shown in Figure 3.1 in the r - θ plane, are expressed as:

$$\frac{\partial \sigma_r}{\partial r} + \frac{1}{r} \frac{\partial \tau_{r\theta}}{\partial \theta} + \frac{\partial \tau_{rz}}{\partial z} + \frac{\sigma_r - \sigma_\theta}{r} = 0 \quad 3.1$$

$$\frac{\partial \tau_{rz}}{\partial r} + \frac{1}{r} \frac{\partial \tau_{\theta z}}{\partial \theta} + \frac{\partial \sigma_z}{\partial z} + \frac{\tau_{rz}}{r} = 0 \quad 3.2$$

$$\frac{\partial \tau_{r\theta}}{\partial r} + \frac{1}{r} \frac{\partial \sigma_\theta}{\partial \theta} + \frac{\partial \tau_{\theta z}}{\partial z} + \frac{2\tau_{r\theta}}{r} = 0 \quad 3.3$$

where τ denotes shear stress and σ denotes total normal stress. The symbols " r ," " θ ," and " z "

indicate the radial, circumferential, and axial directions, respectively. Compressive stresses are considered positive.

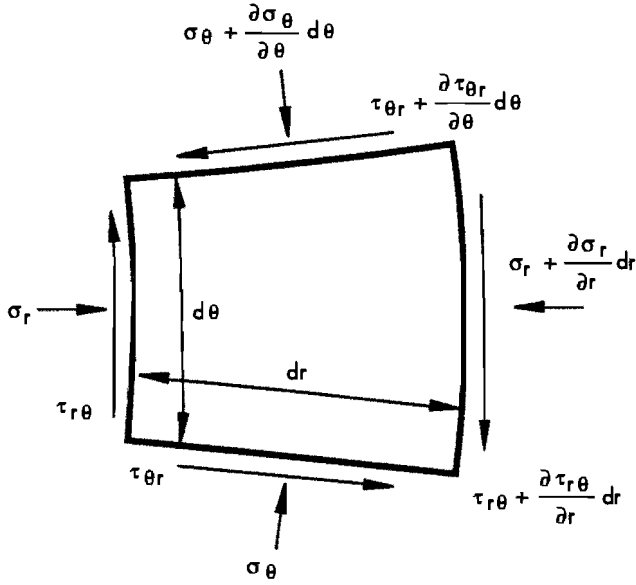


Figure 3.1 Elemental volume of soil showing plane-strain equilibrium stresses

Plane strain deformation requires that all derivatives with respect to the z direction be zero. The axial symmetry of the specimen geometry also requires that there be no variation of displacements or stresses in the θ direction, and the circumferential displacement, v , is zero. Applying these conditions to the equilibrium equations yields one equation that describes the equilibrium of the element in the radial direction:

$$\frac{\partial \sigma_r}{\partial r} + \frac{\sigma_r - \sigma_\theta}{r} = 0 \quad 3.4$$

This equation involves two stresses, the radial stress and the circumferential stress.

The equilibrium equation, 3.4, can also be expressed in terms of displacements. This is done by relating the elemental strains to the effective stresses using Hooke's Law:

$$\epsilon_r = \frac{1}{E} [\bar{\sigma}_r - \nu \bar{\sigma}_\theta - \nu \bar{\sigma}_z] \quad 3.5$$

$$\epsilon_\theta = \frac{1}{E} [-\nu \bar{\sigma}_r + \bar{\sigma}_\theta - \nu \bar{\sigma}_z] \quad 3.6$$

$$\epsilon_z = \frac{1}{E} [-\nu \bar{\sigma}_r - \nu \bar{\sigma}_\theta + \bar{\sigma}_z] \quad 3.7$$

where ϵ denotes strain and $\bar{\sigma}$ denotes effective stress. Compressive stresses and strains are considered positive. Strains are expressed in terms of displacements by:

$$\epsilon_r = -\frac{\partial u}{\partial r} \quad 3.8$$

$$\epsilon_\theta = -\frac{u}{r} - \frac{1}{r} \frac{\partial v}{\partial \theta} \quad 3.9$$

$$\epsilon_z = -\frac{\partial w}{\partial z} \quad 3.10$$

where

- u = radial displacement
- v = circumferential displacement
- w = axial displacement

Invoking Terzaghi's principle of effective stress, the effective stress ($\bar{\sigma}$) is equal to the total stress (σ) minus the pore water pressure (p): $\bar{\sigma} = \sigma - p$. Thus, Equations 3.5, 3.6, and 3.7 can be written in terms of total stresses as:

$$\epsilon_r = \frac{1}{E} [\sigma_r - \nu \sigma_\theta - \nu \sigma_z] - \frac{(1-2\nu)}{E} p \quad 3.11$$

$$\epsilon_\theta = \frac{1}{E} [-\nu \sigma_r + \sigma_\theta - \nu \sigma_z] - \frac{(1-2\nu)}{E} p \quad 3.12$$

$$\epsilon_z = \frac{1}{E} [-\nu \sigma_r - \nu \sigma_\theta + \sigma_z] - \frac{(1-2\nu)}{E} p \quad 3.13$$

Inverting Equations 3.11-3.13 to give stresses in terms of strains and pore water pressure yields:

$$\sigma_r = \frac{E}{(1-2\nu)(1+\nu)} [(1-\nu)\epsilon_r + \nu\epsilon_\theta + \nu\epsilon_z] + p \quad 3.14$$

$$\sigma_\theta = \frac{E}{(1-2\nu)(1+\nu)} [\nu\epsilon_r + (1-\nu)\epsilon_\theta + \nu\epsilon_z] + p \quad 3.15$$

$$\sigma_z = \frac{E}{(1-2\nu)(1+\nu)} [\nu\epsilon_r + \nu\epsilon_\theta + (1-\nu)\epsilon_z] + p \quad 3.16$$

Substituting these expressions into the equilibrium equation, Equation 3.4, with $\epsilon_z = 0$ and simplifying gives:

$$\frac{(1-\nu)}{(1-2\nu)} \frac{\partial \epsilon_r}{\partial r} + \frac{\nu}{(1-2\nu)} \frac{\partial \epsilon_\theta}{\partial r} + \frac{(1+\nu)}{E} \frac{\partial p}{\partial r} + \frac{1}{r}(\epsilon_r - \epsilon_\theta) = 0 \quad 3.17$$

The condition of plane strain and the axial symmetry of the specimen geometry and surface loads reduce the expressions for strains. Equations 3.8, 3.9, and 3.10 can be written as:

$$\epsilon_r = -\frac{\partial u}{\partial r} \quad 3.18$$

$$\epsilon_\theta = -\frac{u}{r} \quad 3.19$$

$$\epsilon_z = 0 \quad 3.20$$

Substitution of Equations 3.18 through 3.20 into the equilibrium equation, 3.17, and simplifying yields:

$$\left[\frac{\partial^2 u}{\partial r^2} + \frac{1}{r} \frac{\partial u}{\partial r} - \frac{u}{r^2} \right] - \frac{(1-2\nu)(1+\nu)}{(1-\nu)E} \frac{\partial p}{\partial r} = 0 \quad 3.21$$

This equation represents the equilibrium equation in terms of displacements and pore water pressures. The equation contains two unknowns, u and p . A second equation is required to solve for the unknowns.

3.4 FLOW EQUATION

The second governing equation is derived by applying Darcy's Law to the flow of water through an infinitesimal element like the one shown in Figure 3.2. Flow out of the element is considered positive. The stipulation that the soil is saturated and remains saturated requires that the change in volume of the element is equal to the net volume of water moving out of the element. If q is the flow rate, where $q = -k_r i A$, according to Darcy's Law, then the rate of change of volume of the element with respect to time is:

$$\frac{dV}{dt} = \frac{dV_w}{dt} = q_{out} - q_{in} = \frac{\partial q}{\partial r} dr \quad 3.22$$

where V is the volume of the element, V_w is the volume of water in the element, and q_{out} and q_{in} are the flow rates out of and into the element, respectively.

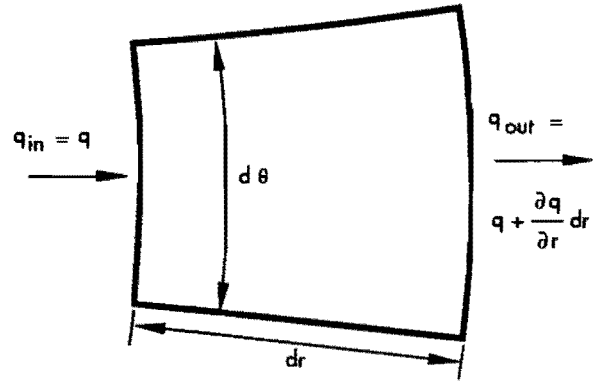


Figure 3.2 Elemental volume of soil showing net flow of water through element

The gradient, i , is expressed by:

$$i = \frac{1}{\gamma_w} \frac{\partial p}{\partial r} \quad 3.23$$

Substituting Equation 3.23 into Darcy's Law gives:

$$q = -\frac{k_r}{\gamma_w} \frac{\partial p}{\partial r} A \quad 3.24$$

Thus, Equation 3.22 can be written as:

$$\begin{aligned} \frac{dV}{dt} &= \frac{\partial}{\partial r} \left[-\frac{k_r}{\gamma_w} \frac{\partial p}{\partial r} A \right] dr \\ &= -\frac{k_r}{\gamma_w} \left[\frac{\partial^2 p}{\partial r^2} A + \frac{\partial p}{\partial r} \frac{\partial A}{\partial r} \right] dr \end{aligned} \quad 3.25$$

Substituting the cross-sectional area of the element, $A = r d\theta dz$, into Equation 3.25 and simplifying produces:

$$\begin{aligned} \frac{dV}{dt} &= -\frac{k_r}{\gamma_w} \left[\frac{\partial^2 p}{\partial r^2} r dr d\theta dz + \frac{\partial p}{\partial r} dr d\theta dz \right] \\ &= -\frac{k_r}{\gamma_w} \left[\frac{\partial^2 p}{\partial r^2} + \frac{1}{r} \frac{\partial p}{\partial r} \right] V_o \end{aligned} \quad 3.26$$

where $V_o = r dr d\theta dz$.

An expression which describes the rate of change of the volume of the element in terms of the radial displacement is required to couple the displacement and pore water pressure. This is obtained by considering the volumetric strain of the element caused by the radial displacement. The volumetric strain, defined as the change in volume of the element divided by the initial volume of the element, is equal to the sum of the linear strains (Note: $\epsilon_z = 0$):

$$\epsilon_{vol} = \frac{dV}{V_0} = \epsilon_r + \epsilon_\theta \quad 3.27$$

Solving Equation 3.25 for dV and differentiating with respect to time gives:

$$\frac{dV}{dt} = \left(\frac{\partial \epsilon_r}{\partial t} + \frac{\partial \epsilon_\theta}{\partial t} \right) V_0 \quad 3.28$$

Substituting the expressions for strain, Equations 3.18, 3.19, and 3.20, into Equation 3.28 yields:

$$\frac{dV}{dt} = - \left[\frac{\partial^2 u}{\partial t \partial r} + \frac{1}{r} \frac{\partial u}{\partial t} \right] V_0 \quad 3.29$$

The rate of change of volume of the element given by Equations 3.26 and 3.29 must be the same. Thus:

$$-V_0 \left[\frac{\partial^2 u}{\partial t \partial r} + \frac{1}{r} \frac{\partial u}{\partial t} \right] = - \frac{k_r}{\gamma_w} \left[\frac{\partial^2 p}{\partial r^2} + \frac{1}{r} \frac{\partial p}{\partial r} \right] V_0$$

or,

$$\frac{\partial^2 u}{\partial t \partial r} + \frac{1}{r} \frac{\partial u}{\partial t} = \frac{k_r}{\gamma_w} \left[\frac{\partial^2 p}{\partial r^2} + \frac{1}{r} \frac{\partial p}{\partial r} \right] \quad 3.30$$

3.5 SUMMARY

The consolidation of a cylindrical specimen of saturated clay due to drying at the surface is a coupled process which depends on both the pore water pressure and radial displacement of the soil. The two governing partial differential equations are derived from the conditions of equilibrium and continuity of flow through the element. The coupling of equations is achieved by recognizing that the rate of change of volume of the element due to an increase in effective stress is equal to the rate of volume change associated with the removal of pore water from the element. The governing partial differential equations are:

$$\left[\frac{\partial^2 u}{\partial r^2} + \frac{1}{r} \frac{\partial u}{\partial r} - \frac{u}{r^2} \right] - \frac{(1-2\nu)(1+\nu)}{(1-\nu)E} \frac{\partial p}{\partial r} = 0 \quad 3.31$$

and

$$\frac{\partial^2 u}{\partial t \partial r} + \frac{1}{r} \frac{\partial u}{\partial t} = \frac{k_r}{\gamma_w} \left[\frac{\partial^2 p}{\partial r^2} + \frac{1}{r} \frac{\partial p}{\partial r} \right] \quad 3.32$$

A finite element formulation for solving these equations is presented in the following chapter.

CHAPTER 4. FINITE ELEMENT FORMULATION

4.1 INTRODUCTION

The coupled partial differential equations of equilibrium and flow developed in Chapter 3 were solved using a finite element formulation. The finite element formulation uses one-dimensional linear elements with two nodes in the radial direction. The one-dimensional elements allow for easy assembly of the stiffness matrices. The time-stepping scheme is a forward difference technique which makes the solution of the coupled equations relatively straightforward. Element stresses are evaluated at the midpoint of each element at regular time intervals during the solution.

4.2 DISCRETIZATION

The one-dimensional finite element with two nodes is pictured in Figure 4.1. The value of displacement or pore water pressure at any point along the element is described as a function of the nodal values of the displacement or pore water pressure. The discretization is expressed as:

$$\mathbf{u}^{(e)} = [N_1 N_2] \begin{bmatrix} u_1^{(e)} \\ u_2^{(e)} \end{bmatrix} = \mathbf{N}^T \mathbf{U}^{(e)} \quad 4.1a$$

$$\mathbf{p}^{(e)} = [N_1 N_2] \begin{bmatrix} p_1^{(e)} \\ p_2^{(e)} \end{bmatrix} = \mathbf{N}^T \mathbf{P}^{(e)} \quad 4.1b$$

The terms N_1 and N_2 represent the element shape functions which define how the displacements and pore water pressures vary along the element. The shape functions are expressed as:

$$N_1 = \frac{r_2 - r}{r_2 - r_1} \quad 4.2$$

$$N_2 = \frac{r - r_1}{r_2 - r_1}$$

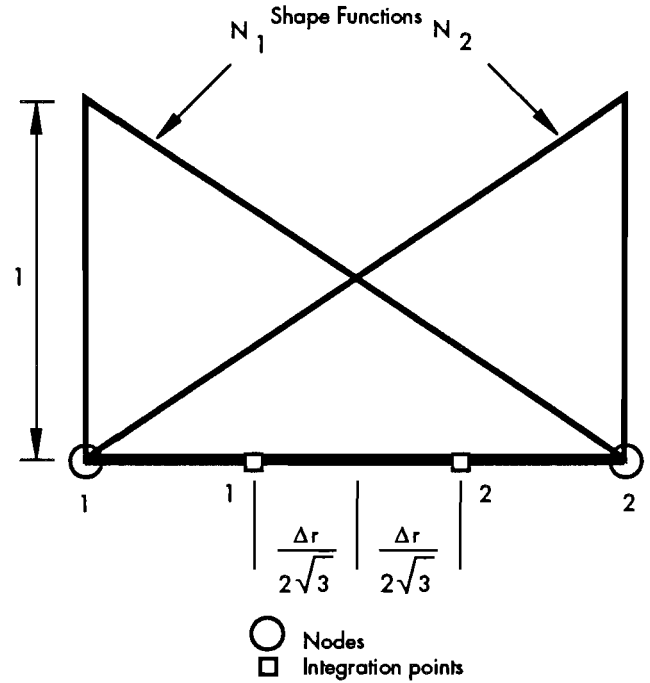


Figure 4.1 One-dimensional finite element with two nodes showing linear shape functions and location of integration points

The shape functions are defined in terms of the global coordinate system.

4.3 PRINCIPLE OF VIRTUAL WORK

The finite element equations which are solved to determine displacements and pore pressures are variational (weak) statements of the governing partial differential equations which were developed in Chapter 3. The weak form of each equation is obtained by applying the Principle of Virtual Work to that equation. A general statement of the Principle of Virtual Work implies that the total internal work done in making an arbitrary virtual change in displacement (or pore pressure) is balanced by the external work done along the boundary of an element due to the arbitrary change. This is applied to both the equilibrium equation and the flow equation.

4.3.1 Equilibrium Equation

Neglecting inertia and body forces, the variational form of the equilibrium equation is:

$$\int_{\Omega} \delta \boldsymbol{\varepsilon}^T \boldsymbol{\sigma} d\Omega = \int_{\Gamma_t} \delta \mathbf{u}^T \mathbf{T} d\Gamma_t \quad 4.3$$

where

- Ω = the domain (two-dimensional cross-section): the r - θ plane;
- Γ_t = the traction boundary (circumference of specimen): $2\pi r$;
- $\delta \boldsymbol{\varepsilon}^T$ = strains due to virtual displacement;
- $\boldsymbol{\sigma}$ = total stress on the element;
- $\delta \mathbf{u}$ = virtual displacement; and
- \mathbf{T} = boundary tractions.

The term on the right-hand side of Equation 4.3 gives rise to equivalent nodal forces at the ends of each element. During assembly of the total matrix equations, when the contributions of the different elements are combined, the resultants of these equivalent nodal forces must equal the external applied loads, which are zero for the present analyses. Thus, writing the equivalent nodal forces as $\delta \mathbf{U}^{(e)T} \mathbf{R}^{(e)}$, the forces can be neglected in the following derivation because they will later cancel during assembly of the global equations. Expanding the integral in Equation 4.3 and writing the equation for an individual element gives:

$$\int_0^{2\pi} \int_{r_1}^{r_2} \delta \boldsymbol{\varepsilon}^T \boldsymbol{\sigma} r dr d\theta = \delta \mathbf{U}^{(e)T} \mathbf{R}^{(e)} \quad 4.4$$

Recalling the expressions for stress and strain from Chapter 4, in matrix notation:

$$\boldsymbol{\sigma} = \begin{bmatrix} \sigma_r \\ \sigma_\theta \end{bmatrix} = \frac{E}{(1-2\nu)(1+\nu)} \begin{bmatrix} 1-\nu & \nu \\ \nu & 1-\nu \end{bmatrix} \begin{bmatrix} \varepsilon_r \\ \varepsilon_\theta \end{bmatrix} + p \begin{bmatrix} 1 \\ 1 \end{bmatrix} = \mathbf{D} \boldsymbol{\varepsilon} + \mathbf{m} p \quad 4.5$$

where

$$\mathbf{D} = \frac{E}{(1-2\nu)(1+\nu)} \begin{bmatrix} 1-\nu & \nu \\ \nu & 1-\nu \end{bmatrix}$$

$$\mathbf{m} = \begin{bmatrix} 1 \\ 1 \end{bmatrix}$$

and

$$\boldsymbol{\varepsilon} = \begin{bmatrix} \varepsilon_r \\ \varepsilon_\theta \end{bmatrix} = \begin{bmatrix} -\frac{\partial}{\partial r} \\ -\frac{1}{r} \end{bmatrix} \mathbf{u} \quad 4.6$$

Substituting the finite element approximations in Equations 4.1 into Equation 4.6 gives:

$$\boldsymbol{\varepsilon} = \begin{bmatrix} -\frac{\partial}{\partial r} \\ -\frac{1}{r} \end{bmatrix} \begin{bmatrix} N_1 N_2 \end{bmatrix} \begin{bmatrix} u_1^{(e)} \\ u_2^{(e)} \end{bmatrix} = \begin{bmatrix} -\frac{\partial N_1}{\partial r} & -\frac{\partial N_2}{\partial r} \\ -\frac{N_1}{r} & -\frac{N_2}{r} \end{bmatrix} \begin{bmatrix} u_1^{(e)} \\ u_2^{(e)} \end{bmatrix} = \mathbf{B} \mathbf{U}^{(e)} \quad 4.7$$

where

$$\mathbf{B} = \begin{bmatrix} -\frac{\partial N_1}{\partial r} & -\frac{\partial N_2}{\partial r} \\ -\frac{N_1}{r} & -\frac{N_2}{r} \end{bmatrix}$$

Introducing Equation 4.7 into Equation 4.5 then gives:

$$\boldsymbol{\sigma} = \mathbf{D} \mathbf{B} \mathbf{U}^{(e)} + \mathbf{m} \mathbf{N}^T \mathbf{P}^{(e)} \quad 4.8$$

Since $\boldsymbol{\varepsilon} = \mathbf{B} \mathbf{U}^{(e)}$ then $\delta \boldsymbol{\varepsilon} = \mathbf{B} \delta \mathbf{U}^{(e)}$ and $\delta \boldsymbol{\varepsilon}^T = \delta \mathbf{U}^{(e)T} \mathbf{B}^T$. Substituting this expression and Equation 4.8 into the equation of virtual work, 4.4, gives:

$$\int_0^{2\pi} \int_{r_1}^{r_2} \delta \mathbf{U}^{(e)T} \mathbf{B}^T \mathbf{D} \mathbf{B} \mathbf{U}^{(e)} r dr d\theta + \int_0^{2\pi} \int_{r_1}^{r_2} \delta \mathbf{U}^{(e)T} \mathbf{B}^T \mathbf{m} \mathbf{N}^T \mathbf{P}^{(e)} r dr d\theta = \delta \mathbf{U}^{(e)T} \mathbf{R}^{(e)} \quad 4.9$$

Integrating with respect to $d\theta$ produces a constant factor of 2π which is eliminated from both sides of the equation. Also, $\delta \mathbf{U}^{(e)T}$, $\mathbf{U}^{(e)}$, and $\mathbf{P}^{(e)}$ are not functions of the radius, so they are moved outside the integral. The term $\delta \mathbf{U}^{(e)T}$ is eliminated from both sides of the equation because it is assumed to be arbitrary and non-zero. The final form of the variational expression of equilibrium for an element is:

$$\left[\int_{r_1}^{r_2} \mathbf{B}^T \mathbf{D} \mathbf{B} r dr \right] \mathbf{U}^{(e)} = - \left[\int_{r_1}^{r_2} \mathbf{B}^T \mathbf{m} \mathbf{N}^T r dr \right] \mathbf{P}^{(e)} + \mathbf{R}^{(e)}$$

or

$$\mathbf{K}^{(e)}\mathbf{U}^{(e)} = -\mathbf{A}^{(e)}\mathbf{P}^{(e)} + \mathbf{R}^{(e)} \quad 4.10$$

Closed-form expressions for the components of the "stiffness" matrices \mathbf{K} and \mathbf{A} are developed in Appendix A.

4.3.2 Flow Equation

The variational form of the flow equation is obtained by multiplying Equation 3.29 by an arbitrary virtual pressure change, δp , which is a non-zero function of r , and then integrating the equation over the domain. This is expressed mathematically as:

$$\int_{r_1}^{r_2} \delta p \left(\dot{u}' + \frac{1}{r} \dot{u} \right) r dr = \frac{k_r}{\gamma_w} \int_{r_1}^{r_2} \left(\delta p p'' + \frac{1}{r} \delta p p' \right) r dr \quad 4.11$$

where the dot ($\dot{\cdot}$) denotes a time derivative and a prime ($'$) denotes a derivative with respect to r . Note also that integration with respect to $d\theta$ yields a constant factor of 2π which has been eliminated from both sides of the equation.

Green's Theorem (integration by parts) is used to reduce the second derivative to a first derivative and the expression is simplified to give:

$$\begin{aligned} \int_{r_1}^{r_2} \delta p (\dot{u}' r dr) + \int_{r_1}^{r_2} \delta p \dot{u} dr + \frac{k_r}{\gamma_w} \int_{r_1}^{r_2} \delta p p' p' r dr \\ = \frac{k_r}{\gamma_w} \delta p p' r \Big|_{r_1}^{r_2} \end{aligned} \quad 4.12$$

Substituting the finite element approximations, Equations 4.1a and 4.1b, into Equation 4.12 gives:

$$\begin{aligned} \int_{r_1}^{r_2} \delta \mathbf{P}^T \mathbf{N} \frac{\partial \mathbf{N}^T}{\partial r} \dot{\mathbf{U}}^{(e)} r dr + \int_{r_1}^{r_2} \delta \mathbf{P}^T \mathbf{N} \mathbf{N}^T \dot{\mathbf{U}}^{(e)} dr \\ + \frac{k_r}{\gamma_w} \int_{r_1}^{r_2} \delta \mathbf{P}^T \frac{\partial \mathbf{N}}{\partial r} \frac{\partial \mathbf{N}^T}{\partial r} \mathbf{P}^{(e)} r dr = \frac{k_r}{\gamma_w} \delta \mathbf{P}^T p' r \Big|_{r_1}^{r_2} \end{aligned} \quad 4.13$$

Noting again that $\delta \mathbf{P}^T$, $\mathbf{P}^{(e)}$ and $\dot{\mathbf{U}}^{(e)}$ are not functions of the radius, they are moved outside the integrals, and $\delta \mathbf{P}^T$ is eliminated from each side of the equation to give:

$$\begin{aligned} \left[\int_{r_1}^{r_2} \mathbf{N} \frac{\partial \mathbf{N}^T}{\partial r} r dr \right] \dot{\mathbf{U}}^{(e)} + \left[\int_{r_1}^{r_2} \mathbf{N} \mathbf{N}^T dr \right] \dot{\mathbf{U}}^{(e)} \\ + \frac{k_r}{\gamma_w} \left[\int_{r_1}^{r_2} \frac{\partial \mathbf{N}}{\partial r} \frac{\partial \mathbf{N}^T}{\partial r} r dr \right] \mathbf{P}^{(e)} = \frac{k_r}{\gamma_w} \frac{\partial p}{\partial r} r \Big|_{r_1}^{r_2} \end{aligned}$$

or

$$\mathbf{C}^{(e)} \dot{\mathbf{U}}^{(e)} + \mathbf{F}^{(e)} \mathbf{P}^{(e)} = \mathbf{Q}^{(e)} \quad 4.14$$

The term $\mathbf{Q}^{(e)}$ is a vector containing the flow at each node. The "stiffness" matrices $\mathbf{C}^{(e)}$ and $\mathbf{F}^{(e)}$ are developed in Appendix A.

4.4 SOLUTION PROCEDURE

The finite element equations presented above apply to individual mesh elements. The individual element matrices are assembled into global matrices according to the connectivity of the mesh elements. A typical finite element mesh used to represent the cylindrical clay specimen is shown in Figure 4.2. Because the one-dimensional elements are connected only at the end nodes, the global "stiffness" matrices are banded, with a band width of three. The global finite element equations are of the same form as those for each element except that, as already discussed, the resultant of the equivalent forces $\mathbf{R}^{(e)}$ must be zero; thus:

$$\mathbf{K}\mathbf{U} = -\mathbf{A}\mathbf{P} \quad 4.15$$

$$\mathbf{C}\dot{\mathbf{U}} + \mathbf{F}\mathbf{P} = \mathbf{Q} \quad 4.16$$

where \mathbf{K} , \mathbf{A} , \mathbf{F} , and \mathbf{C} are square ($n \times n$) matrices and \mathbf{U} , $\dot{\mathbf{U}}$, \mathbf{P} , and \mathbf{Q} are vectors ($n \times 1$), where n is the number of nodes in the global mesh.

The solution of this system of equations is relatively straight forward. First, the equilibrium equation is solved for \mathbf{U} :

$$\mathbf{U} = -\mathbf{K}^{-1}\mathbf{A}\mathbf{P} \quad 4.17$$

Noting that $\dot{\mathbf{U}} = -\mathbf{K}^{-1}\mathbf{A}\dot{\mathbf{P}}$, the expression for $\dot{\mathbf{U}}$ is substituted into the flow equation (4.16) to give:

$$\mathbf{C}(-\mathbf{K}^{-1}\mathbf{A}\dot{\mathbf{P}}) + \mathbf{F}\mathbf{P} = \mathbf{Q} \quad 4.18$$

so

$$\mathbf{P}_{t+\Delta t} = [\mathbf{Z}^{-1}\mathbf{Q} - \mathbf{Z}^{-1}\mathbf{F}\mathbf{P}_t]\Delta t + \mathbf{P}_t \quad 4.20$$

Once the pore water pressures have been determined, they are substituted into the expression for \mathbf{U} to give the displacements at time $t+\Delta t$:

$$\mathbf{U}_{t+\Delta t} = -\mathbf{K}^{-1}\mathbf{A}\mathbf{P}_{t+\Delta t} \quad 4.21$$

4.5 BOUNDARY CONDITIONS

The boundary conditions which must be specified to obtain a solution to Equations 4.16 and 4.17 include the stresses at the surface of the specimen, the flow of water at the surface of the specimen, and the displacement of the axis of the specimen. The surface tractions are zero and have already been incorporated into the equilibrium equation. The axial symmetry of the specimen requires that displacements be zero on the axis of the specimen, represented by node 1 in Figure 4.2; thus, $u_1 = 0$. The flow of water through the specimen is described in Equation 4.16 by the vector \mathbf{Q} , which is the vector of net flow rate across each mesh node resulting from assembly of the equivalent nodal flows from each element:

$$\mathbf{Q}^{(e)} = - \left[\begin{array}{c} \frac{k_r}{\gamma_w} \frac{\partial p}{\partial r} \Big|_{r_2} \\ \frac{k_r}{\gamma_w} \frac{\partial p}{\partial r} \Big|_{r_1} \end{array} \right] \quad 4.22$$

At the axis of the specimen there is no flow of water across the boundary. Thus, the gradient, $\frac{1}{\gamma_w} \frac{\partial p}{\partial r}$, is zero at the axis, and the flow across node 1 is equal to zero, $q_1 = 0$. Also, because water can only be removed from the specimen at the surface, node n in Figure 4.2, the compatibility of flow requires that the net flow across each interior mesh node is zero, so $q_i = 0$ for $1 < i < n$. This implies:

$$\mathbf{Q} = \begin{bmatrix} 0 \\ \cdot \\ \cdot \\ 0 \end{bmatrix} \quad \text{where} \quad q_n = - \left(\frac{k_r}{\gamma_w} \frac{\partial p}{\partial r} R \right) \quad 4.23$$

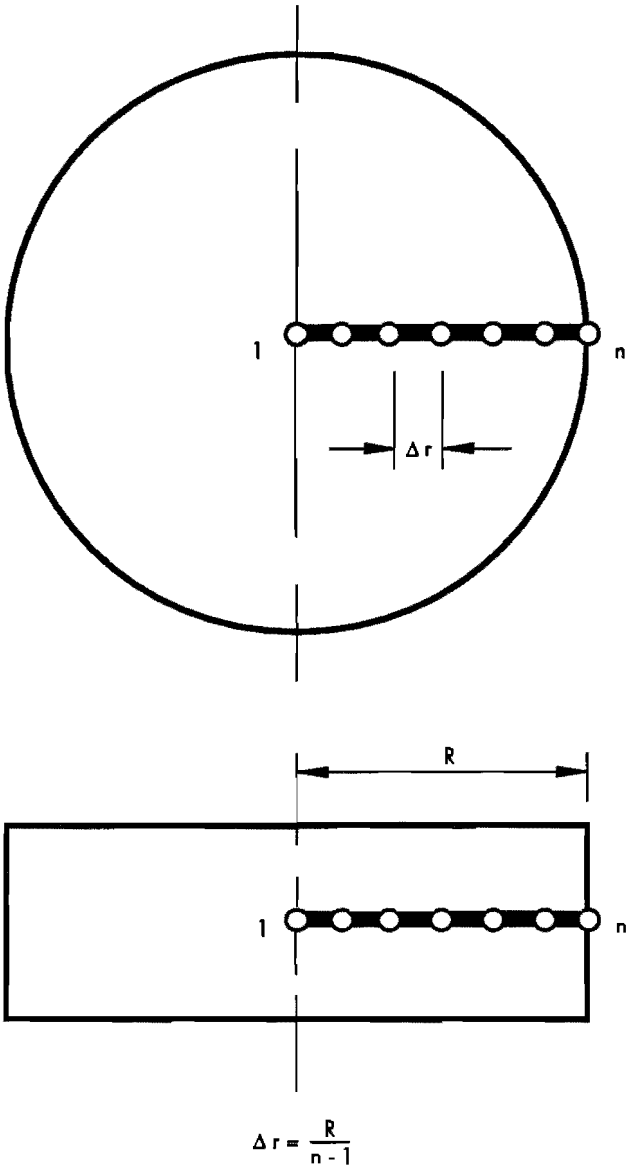


Figure 4.2 Typical mesh of one-dimensional finite elements used to represent a cylindrical clay specimen

Equation 4.18 represents a linear system of first-order differential equations:

$$\mathbf{Z}\dot{\mathbf{P}} + \mathbf{F}\mathbf{P} = \mathbf{Q} \quad 4.19$$

where $\mathbf{Z} = -\mathbf{C}\mathbf{K}^{-1}\mathbf{A}$. Equation 4.19 is solved for $\dot{\mathbf{P}}$ and, then, a forward finite difference approximation is used to determine $\mathbf{P}_{t+\Delta t}$:

$$\dot{\mathbf{P}} = \mathbf{Z}^{-1}\mathbf{Q} - \mathbf{Z}^{-1}\mathbf{F}\mathbf{P} \cong \frac{1}{\Delta t}(\mathbf{P}_{t+\Delta t} - \mathbf{P}_t)$$

There are two distinct surface boundary conditions which can be assumed, as follows:

1. The surface flow rate is known as a function of time, i.e., $q_n(t)$ is known.
2. The pore water pressure is known as a function of time, i.e., $p_n(t)$ is known.

The boundary conditions implemented by the numerical model are illustrated in Figure 4.3.

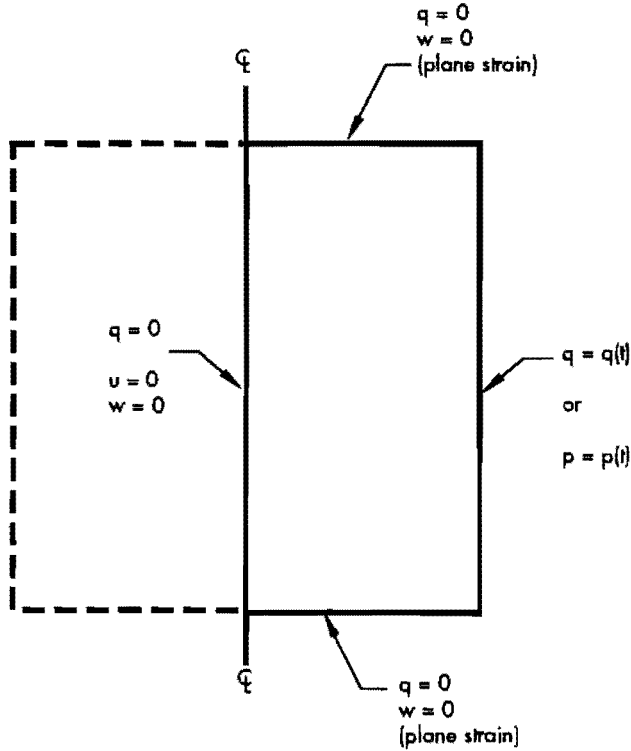


Figure 4.3 Known boundary conditions applied to specimen, including flow and displacement conditions at axis and flow or pore water pressure conditions at surface

For Case 1, where the surface flow rate is known, the solution of Equation 4.20 is relatively simple. At any time, t , the value of $q_n(t)$ is used directly in Equation 4.23 to evaluate \mathbf{Q} , which is then substituted into Equation 4.20 to evaluate the new nodal pore water pressures. For Case 2, where the pore pressure is known, it is necessary to modify the solution procedure because the value of q_n is not known. A solution is obtained by first determining values of p_n and \dot{p}_n . The value of p_n is determined directly from the prescribed boundary curve, $p_n(t)$, while the value of \dot{p}_n is determined by numerically differentiating the boundary curve. It is then possible to reduce

Equation 4.19 to a system of $n-1$ simultaneous linear differential equations which do not include q_n , which is unknown.

Consider Equation 4.19 in expanded form :

$$\begin{aligned} z_{1,1}\dot{p}_1 + \dots + z_{1,n}\dot{p}_n + f_{1,1}p_1 + \dots + f_{1,n}p_n &= 0 \\ \vdots & \\ z_{n-1,1}\dot{p}_1 + \dots + z_{n-1,n}\dot{p}_n + f_{n-1,1}p_1 + \dots + f_{n-1,n}p_n &= 0 \\ z_{n,1}\dot{p}_1 + \dots + z_{n,n}\dot{p}_n + f_{n,1}p_1 + \dots + f_{n,n}p_n &= -q_n \end{aligned} \quad 4.24$$

By excluding the n -th equation, which contains the unknown q_n , from the solution, the remaining system has $n-1$ equations and $n-1$ unknowns, $\dot{p}_1 \dots \dot{p}_{n-1}$ ($p_1 \dots p_n$ are available from the previous time step). All of the known terms, including the known \dot{p}_n terms, are moved to the right-hand side of the equation to give:

$$\begin{aligned} z_{1,1}\dot{p}_1 + \dots + z_{1,n-1}\dot{p}_{n-1} &= -f_{1,1}p_1 - \dots - f_{1,n}p_n - z_{1,n}\dot{p}_n \\ \vdots & \\ z_{n-1,1}\dot{p}_1 + \dots + z_{n-1,n-1}\dot{p}_{n-1} &= -f_{n-1,1}p_1 \\ &\dots - f_{n-1,n}p_n - z_{n-1,n}\dot{p}_n \end{aligned}$$

or

$$\mathbf{Z}^* \dot{\mathbf{P}}^* = -\mathbf{F}^* \mathbf{P} + \dot{p}_n \mathbf{V}^* \quad 4.25$$

where the star (*) indicates a matrix or vector with $n-1$ rows, and

$$\mathbf{V}^* = \begin{bmatrix} -z_{1,n} \\ \vdots \\ -z_{n-1,n} \end{bmatrix}$$

From this point the solution proceeds as before:

$$\dot{\mathbf{P}}^* = -(\mathbf{Z}^*)^{-1} \mathbf{F}^* \mathbf{P} + \dot{p}_n (\mathbf{Z}^*)^{-1} \mathbf{V}^* \equiv \frac{1}{\Delta t} (\mathbf{P}_{t+\Delta t}^* - \mathbf{P}_t^*)$$

and

$$\mathbf{P}_{t+\Delta t}^* = \left[\dot{p}_n (\mathbf{Z}^*)^{-1} \mathbf{V}^* - (\mathbf{Z}^*)^{-1} \mathbf{F}^* \mathbf{P}_t \right] \Delta t + \mathbf{P}_t^* \quad 4.26$$

Equation 4.26, which is solved for pore water pressures when $p_n(t)$ is specified (Case 2), has the same general form as Equation 4.20, which is solved for pore water pressures when $q_n(t)$ is specified (Case 1). The general solution equation is:

$$\mathbf{P}_{t+\Delta t} = \left[(\text{BC})\mathbf{Z}^{-1}\mathbf{X} - \mathbf{Z}^{-1}\mathbf{F}\mathbf{P}_t \right] \Delta t + \mathbf{P}_t \quad 4.27$$

A FORTRAN computer program, SHRINK, was written to implement the finite element solution. The computer program employs Equation 4.27 to solve for nodal pore water pressures. The values of the scalar BC and the vector \mathbf{X} depend upon which boundary condition is in effect. For boundary condition Case 1:

$$\text{BC} = q_n \text{ and } \mathbf{X} = \begin{bmatrix} 0 \\ \vdots \\ -1 \end{bmatrix}_{n \times 1} \quad 4.28$$

such that $\mathbf{Q} = (\text{BC})\mathbf{X}$ in Equation 4.20. For boundary condition Case 2:

$$\text{BC} = \dot{p}_n \text{ and } \mathbf{X}^* = \begin{bmatrix} -z_{1,n} \\ \vdots \\ -z_{n-1,n} \end{bmatrix}_{(n-1) \times 1} \quad 4.29$$

such that $\dot{p}_n \mathbf{V}^* = (\text{BC})\mathbf{X}$ in Equation 4.26. For boundary condition Case 2 the solution considers only $n-1$ terms because the pore water pressure at the surface, p_n , is already known.

4.6 COMPUTATION OF STRESSES

Once displacements and pore water pressures have been determined for a given time step, the stresses in each element are evaluated. This is accomplished by substituting the known displacements and pore water pressures into the expressions for strain and stress, Equations 4.7 and 4.8, respectively. The stresses are calculated only when they are needed for output. Stresses in an element are calculated at the midpoint of the element.

4.7 SUMMARY

A finite element formulation has been developed to model the shrinkage of cylindrical clay specimens due to drying. The finite element formulation uses one-dimensional linear elements described by two nodes. The finite element formulation is developed by applying the Principle of Virtual Work to the governing partial differential equations derived from requirements of static equilibrium and compatibility of flow.

The boundary condition at the surface of the specimen is especially important because it controls the flow of pore water from the interior of the specimen. Two surface boundary conditions are considered: (1) known pore water pressure and (2) known flow rate. The finite element equations result in a banded system of linear differential equations which are solved explicitly using a forward difference formula. Stresses are evaluated at output times based on strains calculated from the nodal displacements.

CHAPTER 5. VERIFICATION OF THEORETICAL MODEL AND COMPUTER PROGRAM

5.1 INTRODUCTION

The computer program SHRINK, which implements the numerical model developed in Chapter 4, was used to perform a series of simulations of the consolidation (shrinkage) of a cylindrical specimen of clay due to drying. The simulations were intended to verify that the numerical solution correctly models consolidation of the soil and to validate the theoretical model. The simulations involved subjecting a cylindrical specimen of clay to a sudden change (decrease) in pore water pressure at the outer boundary. The change in pore water pressure caused the effective stress in the specimen to increase and caused the specimen to consolidate. The ability of the numerical model to simulate consolidation was judged by comparing the average degree of consolidation of the specimen determined by the model with the average degree of consolidation determined according to Terzaghi's theory of consolidation assuming one-dimensional (1-D), two-dimensional (2-D), and three-dimensional (3-D) deformation of the specimen.

5.2 DEGREE OF CONSOLIDATION AND AVERAGE PORE WATER PRESSURE

The average degree of consolidation, at any time t after the beginning of consolidation, was calculated as the ratio of average excess pore water pressure remaining in the soil to the initial average pore water pressure. The average pore water pressure was calculated as an area (volumetric) average to account for the axisymmetric nature of the geometry. The average pore water pressure was evaluated as:

$$\hat{p} = \frac{\int_0^R p \, r \, dr}{\int_0^R r \, dr} \quad 5.1$$

The average excess pore water pressure calculated in this manner will be referred to simply as the average excess pore water pressure in the remainder of this chapter.

5.3 MODELING EFFECTS

The displacement formulation (the Principle of Virtual Work) used to develop the finite element model is a statement of the conservation of energy which states that a system will respond to a change in energy (caused by altered loading) so as to minimize the resulting total potential energy of the system. According to Zienkiewicz and Taylor (1989), the approximation of the minimum potential energy of a system by the finite element method is greater than the true minimum, and it is only equal to the true minimum in the limit as the element size approaches zero. This implies that smaller displacements are required of the approximate system to achieve the minimum potential energy of that system than are required by the real system under the same loading. Thus, the finite element approximation is too "stiff," and it predicts a higher rate of consolidation than the theoretical solution.

The sensitivity of the numerical solution to the number of elements used in the solution was evaluated by computing the displacement of the surface of a specimen subjected to an increase in effective stress of 100 psi using 2, 10, and 20 elements. These results are compared to the exact displacement, determined by elastic theory, in Table 5.1. It can be seen that, even for a finite element mesh with only two elements, the error introduced by the approximation appears to be small.

A comparison of the average degrees of consolidation versus time for a specimen calculated using 2, 10, 20, and 30 elements is shown in Figure 5.1. The results shown in this figure indicate that the number of elements significantly influences the predicted rate of consolidation of the specimen. The percent difference between the average degree of consolidation calculated using 30 elements and the average degree of consolidation

calculated using 2, 10, and 20 elements is shown in Figure 5.2. As the number of elements increases the percent difference is reduced, and for 20 elements the percent difference is seen to be less than 5 percent during most of the consolidation. Based on the results shown in Figures 5.1 and 5.2, 30 finite elements were used to represent the soil specimens in all subsequent analyses.

Table 5.1 Comparison of final diameter of soil specimen subjected to an increase in effective stress of 100 psi calculated by the theory of elasticity and by the finite element solution. Initial diameter: 1.500000 in.

Method of Solution	Final Diameter (in.)
Theory of Elasticity	1.430813
FEM (2 elements)	1.432192
FEM (10 elements)	1.432454
FEM (20 elements)	1.432562
FEM (30 elements)	1.433800

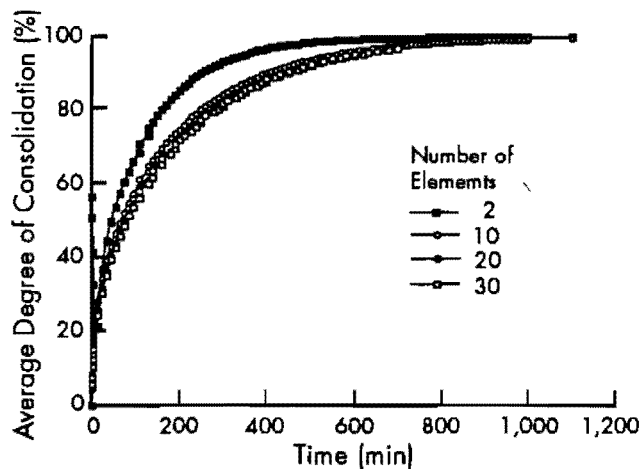


Figure 5.1 Effect of the number of elements on the average degree calculated by the finite element solution. Bulk modulus of elasticity, $K = 1,000$ psi. Poisson's ratio, $\nu = 0.33$

5.4 TERZAGHI'S SOLUTION FOR CONSOLIDATION

According to Terzaghi's classical theory of consolidation, the change in effective stress in a soil which is consolidating will be equal to the change in pore water pressure, provided that there is no change in total stress. For the case of radial flow in a cylindrical specimen, the pore water pressures are governed by the following partial differential equation (Barron, 1948):

$$\frac{\partial p}{\partial t} = c_r \left[\frac{1}{r} \frac{\partial p}{\partial r} + \frac{\partial^2 p}{\partial r^2} \right] \quad 5.2$$

where

- p = excess pore water pressure,
- r = radial distance from an axis of symmetry,
- t = time, and
- c_r = coefficient of consolidation for radial flow.

The soil properties which affect the rate of change of pore water pressure are the hydraulic conductivity, k_r , and the compressibility of the soil skeleton, and these are expressed by c_r (Cryer, 1963) where:

$$c_r = \frac{k_r}{\gamma_w m} \quad 5.3$$

and where γ_w is the unit weight of water and m is the coefficient of volume change of the soil. The coefficient of volume change is a measure of the compressibility of the soil and is defined as the rate of change of volumetric strain of the soil with respect to change in the effective stress (Olson, 1989):

$$m = \frac{d\varepsilon_{vol}}{d\bar{\sigma}} \quad 5.4$$

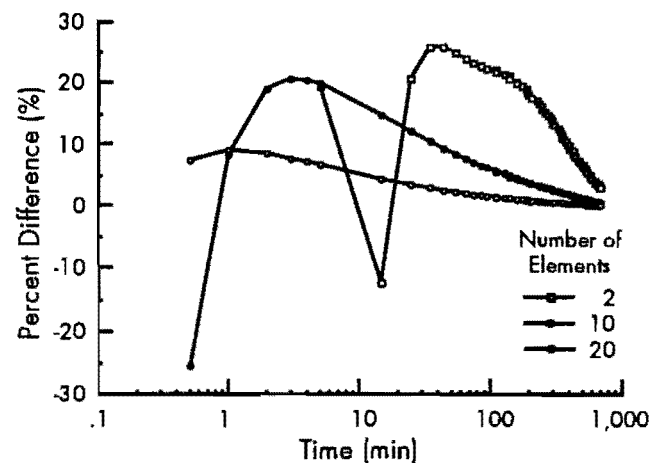


Figure 5.2 Percent difference between the average degree of consolidation calculated using 30 elements and the average degree of consolidation calculated using 2, 10, and 20 elements. Bulk modulus of elasticity, $K = 1,000$ psi. Poisson's ratio, $\nu = 0.33$

Because the excess pore water pressure at a given time varies across the radius of the specimen, it is convenient to define an average degree of consolidation, which is the ratio of the average excess pore water pressure which has been dissipated by consolidation to the initial magnitude of average excess pore water pressure (Olson, 1989):

$$U_r = \frac{\hat{p}_o - \hat{p}}{\hat{p}_o} = 1 - \frac{\hat{p}}{\hat{p}_o} = 1 - \frac{\int_0^R p \, rdr}{\int_0^R p_o \, rdr} \quad 5.5$$

where

- U_r = average degree of consolidation,
- \hat{p} = average excess pore water pressure,
- \hat{p}_o = average initial excess pore water pressure,
- r = radial distance, and
- R = radius of specimen.

An expression relating the average degree of consolidation, U_r , to the time since the beginning of consolidation for radial flow and equal (plane) strain is given by Olson (1989):

$$U_r = 1 - e^{-8T_r} \quad 5.6$$

where T_r is a dimensionless time factor related to the coefficient of consolidation by:

$$T_r = \frac{tc_r}{R^2} \quad 5.7$$

and where t is the time since the beginning of consolidation.

By substituting Equation 5.3 into Equation 5.7, the expression for the time factor becomes:

$$T_r = \frac{k_r}{\gamma_w R^2 m} t \quad 5.8$$

The value of the coefficient of volume change, m , depends on whether the deformation of the material is 1-D (constrained), 2-D (plane strain), or 3-D (isotropic). For each of these three conditions the coefficient of volume change of an elastic material can be expressed in terms of the

bulk modulus of elasticity, K , and Poisson's ratio, ν , of the material as:

$$(m)_{1-D} = \frac{(1 + \nu)}{3K(1 - \nu)} \quad 5.9$$

$$(m)_{2-D} = \frac{2(1 + \nu)}{3K} \quad 5.10$$

$$(m)_{3-D} = \frac{1}{K} \quad 5.11$$

The bulk modulus of elasticity, K , is uniquely related to Young's modulus, E , and Poisson's ratio, ν , by:

$$K = \frac{E}{3(1 - 2\nu)} \quad 5.12$$

For given values of K and ν , Equations 5.9 through 5.11 indicate that

$$(m)_{1-D} < (m)_{2-D} < (m)_{3-D} \quad 5.13$$

Because the time required to reach a given degree of consolidation with radial flow is directly proportional to m (Equation 5.7), consolidation due to one-dimensional deformation is more rapid than that due to two-dimensional deformation, which, in turn, is more rapid than consolidation due to three-dimensional deformation.

5.5 INPUT PARAMETERS

The soil properties selected for the analyses are representative values for the Taylor Marl based on data reported by Kayyal (1986) and Cuenca (1989). The bulk modulus of elasticity, K , was selected as 1,000 psi and the hydraulic conductivity was taken as 1×10^{-8} in./min. Calculations were performed for five values of Poisson's ratio: 0, 0.2, 0.33, 0.4, and 0.48. The specimens used in the analyses had a radius of 0.75 inch and a unit height of 1.0 inch. Thirty finite elements of equal length were used in the radial direction of the specimen, except for Poisson's ratios of 0.2 and 0.4 where it was necessary to use 29 elements to achieve a solution. The initial void ratio of the soil was 0.91, and the initial pore water pressure in the soil was assumed to be zero at all nodes. The increase in effective stress causing consolidation was induced by changing the pore water pressure at the surface of the specimen. The surface pore

pressure was assumed to change from an initial value of 0.0 psi to a value of -100.0 psi in a period of 0.1 minute, after which the pressure remained constant at -100.0 psi until consolidation was completed.

5.6 EVALUATING THE MODEL

The relationship between the average degree of consolidation, U_r , and time, t , calculated by the finite element model was compared to the U_r versus t relationships based on Terzaghi's theory of consolidation. Three relationships between U_r and time were calculated for Terzaghi's theory for each set of elastic constants (K and ν). The three relationships were determined using three coefficients of volume change, based on Equations 5.9 through 5.11, corresponding to 1-D, 2-D, and 3-D deformation. Because the finite element model was developed for the 2-D case of plane strain deformation, the relationship between time and average degree of consolidation determined by the finite element model was expected to compare favorably with Terzaghi's solution determined using the coefficient of volume change computed assuming 2-D deformation.

Figures 5.3 through 5.7 show, for Poisson's ratios of 0, 0.2, 0.33, 0.4, and 0.48, respectively, the relationships between U_r and time as determined by the finite element model and Terzaghi's theory of consolidation assuming 1-D, 2-D, and 3-D deformation. In all cases the finite element solution indicates that the rate of consolidation during the early stages of consolidation is much more rapid than the rate predicted using Terzaghi's theory

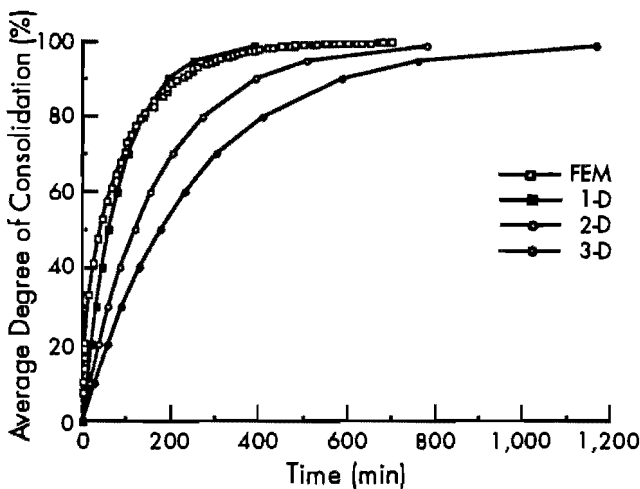


Figure 5.3 Comparison of average degree of consolidation from finite element solution with 1-D, 2-D, and 3-D solutions based on Terzaghi's theory of consolidation. Poisson's ratio, $\nu = 0.0$

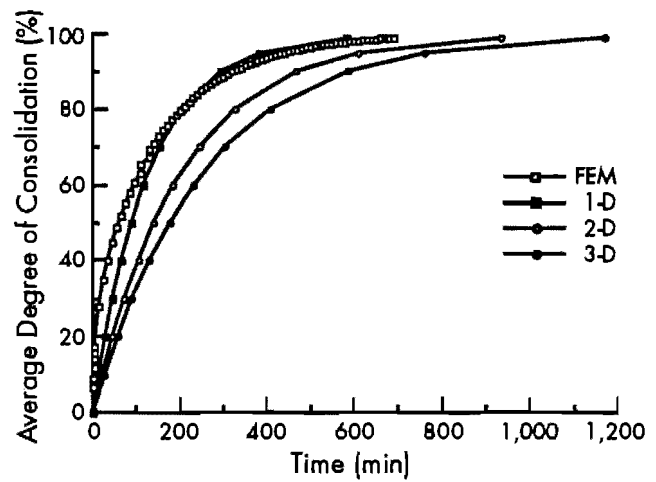


Figure 5.4 Comparison of average degree of consolidation from finite element solution with 1-D, 2-D, and 3-D solutions based on Terzaghi's theory of consolidation. Poisson's ratio, $\nu = 0.20$

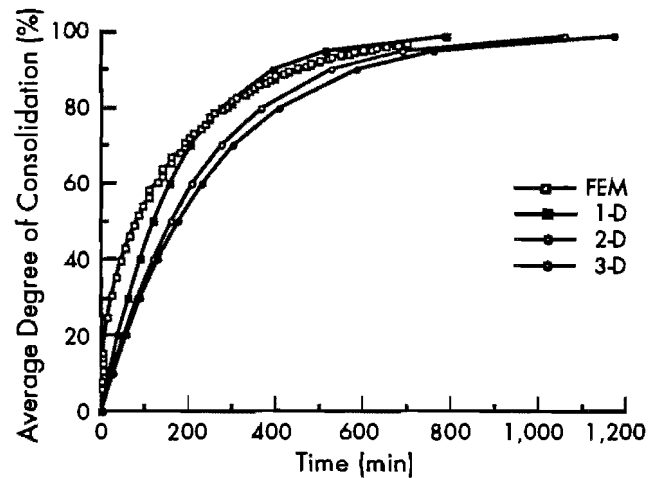


Figure 5.5 Comparison of average degree of consolidation from finite element solution with 1-D, 2-D, and 3-D solutions based on Terzaghi's theory of consolidation. Poisson's ratio, $\nu = 0.33$

with any of the assumed states of deformation. The agreement between the results of the finite element solution and results based on Terzaghi's theoretical solution improves as Poisson's ratio increases, but significant differences exist even when Poisson's ratio is very high. The lack of agreement between the two solutions over such a large range in soil properties (Poisson's ratio) suggests that the differences between the results are not caused by variations in soil properties. Rather, the differences between the results imply that there is a fundamental difference between Terzaghi's theory of consolidation and the finite element model of consolidation developed in Chapter 4.

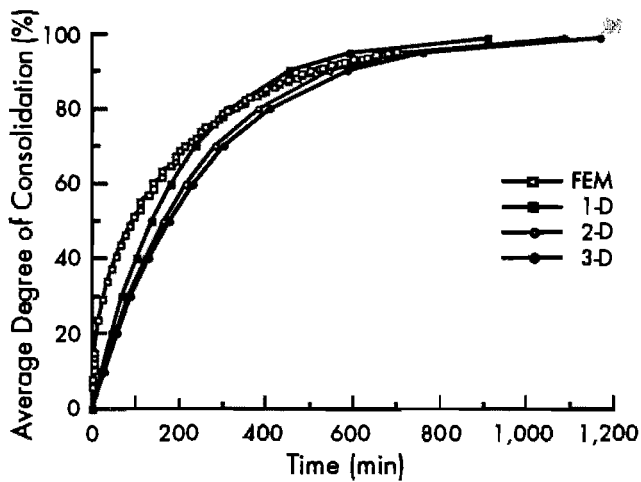


Figure 5.6 Comparison of average degree of consolidation from finite element solution with 1-D, 2-D, and 3-D solutions based on Terzaghi's theory of consolidation. Bulk modulus of elasticity, $K = 1,000$ psi. Poisson's ratio, $\nu = 0.4$

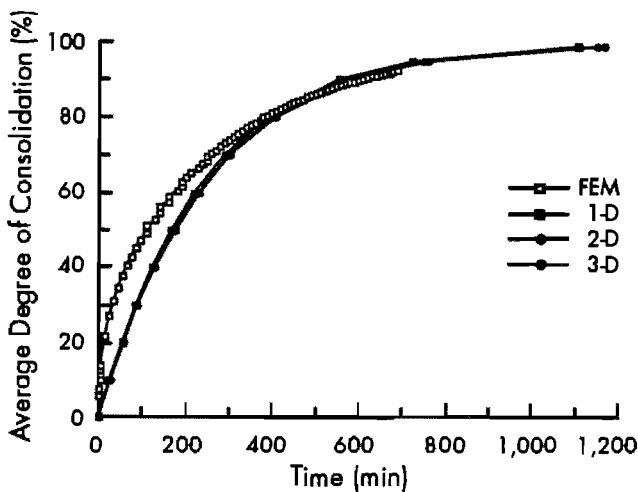


Figure 5.7 Comparison of average degree of consolidation from finite element solution with 1-D, 2-D, and 3-D solutions based on Terzaghi's theory of consolidation. Bulk modulus of elasticity, $K = 1,000$ psi. Poisson's ratio, $\nu = 0.48$

5.7 THE MANDEL-CRYER EFFECT

The differences between the soil response predicted by the finite element model and Terzaghi's theory of consolidation lie in the way in which the two solutions relate changes in stress to changes in volume. The finite element solution fully couples the stresses and deformations, such that the deformation may cause changes in total stress which are not associated with changes in external

loads. In contrast, Terzaghi's solution uncouples the stress and deformation by assuming that when no change occurs in external loads there is no change in total stress; all changes in effective stress are due to changes in pore water pressure. Hwang et al. (1971) suggest that the coupled nature of stress and deformation in a real specimen causes an increase in pore water pressure during the early stages of consolidation after boundary loading has ceased. This effect was noted by Mandel (1953) and Cryer (1963) and is now called the Mandel-Cryer effect (Hwang et al., 1971).

The state of total stress in the drying specimen is illustrated in Figures 5.8 and 5.9, which show the radial total stress and circumferential total stress, respectively, at different times during consolidation. In the early stages of drying, a compressive total stress develops in the interior of the specimen as the outer surface shrinks inward, around the wetter core, in response to rapid volume change at the outer surface of the specimen. This compressive stress causes the pore water pressure in the interior of the specimen, away from the surface, to increase during the early stages of the drying process, as shown in Figure 5.10. The increase in pore water pressure creates an increase in the pressure gradient which accelerates the flow of water to the surface. Because the finite element solution can accurately account for the increased pore water pressure gradient caused by the "squeezing" effect of the consolidating soil, the rate of consolidation predicted by the finite element solution is initially much faster than the rate predicted by the solution based on Terzaghi's theory.

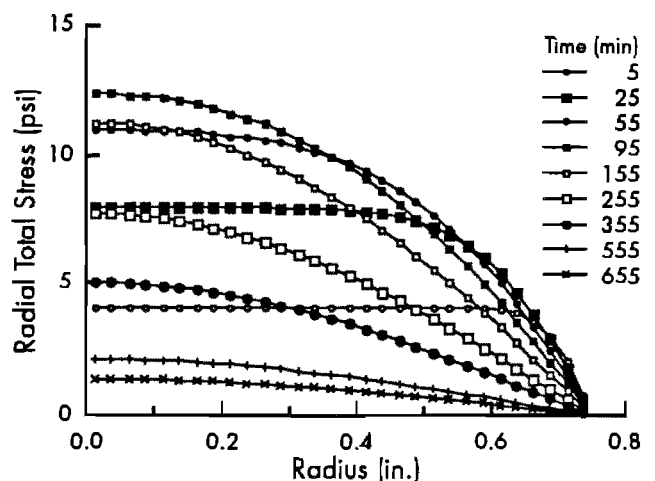


Figure 5.8 Radial distribution of radial total stress at different times due to consolidation caused by drying. Bulk modulus of elasticity, $K = 1,000$ psi. Poisson's ratio, $\nu = 0.33$

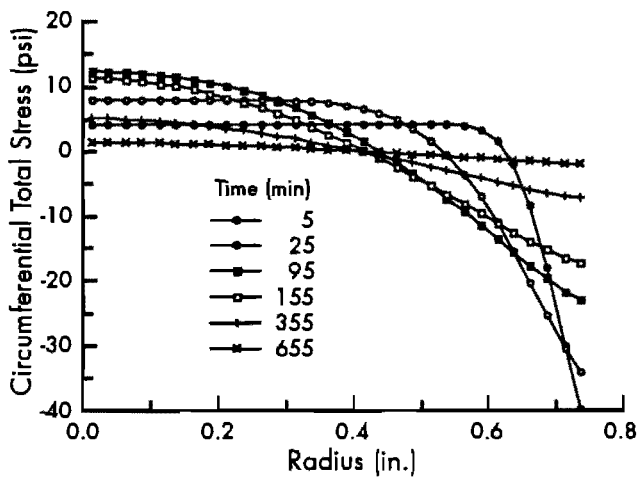


Figure 5.9 Radial distribution of circumferential total stress at different times due to consolidation caused by drying. Bulk modulus of elasticity, $K = 1,000$ psi. Poisson's ratio, $\nu = 0.33$

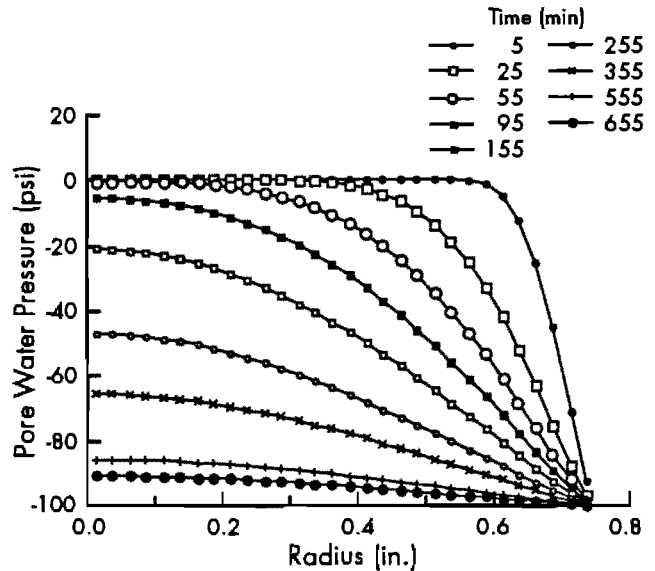


Figure 5.10 Radial distribution of pore water pressure at different times due to consolidation caused by drying. Bulk modulus of elasticity, $K = 1,000$ psi. Poisson's ratio, $\nu = 0.33$

5.8 SUMMARY

The theoretical model and computer program developed in this study were used to determine the relationship between time and average degree of consolidation due to radial flow. Five different values of Poisson's ratio were considered. A degree of consolidation versus time relationship was computed for each of the five values of Poisson's ratio and compared to values determined based on Terzaghi's theory of consolidation using corresponding soil properties.

Qualitatively, the finite element solution appeared to model consolidation behavior correctly. However, significant differences were observed between the finite element solution and the solution based on Terzaghi's theory of consolidation. The difference between the two solutions is believed to result from the manner in which the two solutions relate the state of stress in the soil to

the deformation during consolidation. The finite element solution more fully couples the multi-dimensional stress and deformation and therefore more accurately models the consolidation phenomena than does the solution based on Terzaghi's theory of consolidation.

The finite element model predicts an early increase in pore water pressure in the interior of the specimen during consolidation. This effect is known as the Mandel-Cryer effect and is caused by changes in the total stress in the soil during consolidation. The finite element solution is believed to adequately model the behavior of a cylindrical specimen of clay during drying as long as the specimen remains saturated and appropriate properties are used for hydraulic conductivity, bulk modulus of elasticity, and Poisson's ratio.

CHAPTER 6. NUMERICAL RESULTS OF DRYING SIMULATIONS

6.1 INTRODUCTION

A series of computations was performed using program SHRINK to study the effects of different rates of drying on the behavior of cylindrical specimens of clay. The soil properties for Taylor clay, described previously in Chapter 5, were used for these simulations. Results of these calculations were examined to determine the relationship between the rate of drying and the development of tensile stresses and, thus, cracking in the soil. The effect of the rate of drying on producing tensile stresses in the circumferential direction near the surface of the specimen was of particular interest because the magnitude of the tensile stress should be an indication of the potential for cracking of the specimen. The effect of Poisson's ratio on the state of stress in the specimen was also considered.

6.2 MODELING EFFECTS

The two parameters that are likely to affect the accuracy of the numerical solution are the number of finite elements and the magnitude of the time step used. Suitable values were selected for each to reduce the possibility of errors.

6.2.1 Number of Elements

In Section 5.2 it was shown that 30 finite elements were sufficient to obtain acceptably accurate results from a simulation of consolidation of a specimen during drying. Based on this information, 30 finite elements were used in the studies presented in this chapter.

6.2.2 Time Step

The influence of the time step used in the numerical solution was evaluated by using several different time steps. Three time steps were considered: 0.001 min., 0.0001 min., and 0.00002 min.

The soil specimen had the same characteristics as those used in the study of consolidation discussed in Chapter 5. Poisson's ratio was 0.33.

The rate of drying increased from zero, at the start of drying, to a maximum of 0.0019 in.³/min. after 0.1 minute and remained constant until the end of the period of interest, 1.0 minute. Typical results for the three time steps are summarized in Table 6.1 which lists the displacements and pore water pressures calculated at equidistant points across the radius of the specimen after 0.5 minutes of drying. The results indicate that the time step had no significant effect on the computed results.

6.3 SPECIMEN CHARACTERISTICS AND RATES OF DRYING

The soil properties and specimen geometry used to study the effect of the rate of drying were the same as those used in Chapter 5. A specified rate of drying (flow) was used as the boundary condition at the outer surface. Three rates of drying were selected after examining measured rates of water loss from laboratory specimens of Taylor Marl reported by Kayyal (1986). His data are shown in Figure 6.1. The three rates selected were 0.028 in.³/min., 0.0057 in.³/min., and 0.0019 in.³/min. which are designated as High, Medium, and Low, respectively.

The boundary condition applied at the surface of the specimens assumed the rate of drying increased from zero, at the beginning of drying, to the selected value in a period of 0.1 minutes, after which the rate remained constant until the end of drying. The end of drying was taken to be the time at which one of the following two conditions was met: (1) the calculated volume change of any individual element became greater than the initial volume of void space in the element, or (2) the magnitude of soil suction exceeded 2,000 psi, which is considered to be an approximate upper bound of maximum air-entry suction for clays (Olson, 1990).

Table 6.1 Effect of time step on the displacements and pore water pressures calculated by the finite element method

Time Step (min)	0.001		0.0001		0.00002	
	Displacement (in.)	Pore Water Pressure (psi)	Displacement (in.)	Pore Water Pressure (psi)	Displacement (in.)	Pore Water Pressure (psi)
0.01875	4.60E-09	1.70E-01	4.46E-09	1.70E-01	4.45E-09	1.70E-01
0.05625	2.14E-09	1.71E-01	2.15E-09	1.71E-01	2.15E-09	1.71E-01
0.09375	-2.93E-09	1.71E-01	-2.92E-09	1.70E-01	-2.92E-09	1.70E-01
0.13125	4.20E-09	1.71E-01	4.14E-09	1.71E-01	4.14E-09	1.71E-01
0.16875	-5.13E-09	1.70E-01	-5.01E-09	1.69E-01	-5.00E-09	1.69E-01
0.20625	4.56E-09	1.73E-01	4.38E-09	1.72E-01	4.37E-09	1.72E-01
0.24375	-8.29E-10	1.69E-01	-6.48E-10	1.69E-01	-6.32E-10	1.69E-01
0.28125	-7.81E-09	1.72E-01	-7.91E-09	1.72E-01	-7.92E-09	1.72E-01
0.31875	2.21E-08	1.72E-01	2.20E-08	1.72E-01	2.20E-08	1.72E-01
0.35625	-3.90E-08	1.65E-01	-3.86E-08	1.65E-01	-3.86E-08	1.65E-01
0.39375	4.80E-08	1.83E-01	4.73E-08	1.83E-01	4.72E-08	1.83E-01
0.43125	-2.52E-08	1.54E-01	-2.42E-08	1.54E-01	-2.41E-08	1.54E-01
0.46875	-6.92E-08	1.83E-01	-6.98E-08	1.83E-01	-6.99E-08	1.83E-01
0.50625	2.77E-07	1.86E-01	2.77E-07	1.86E-01	2.77E-07	1.86E-01
0.54375	-5.84E-07	8.92E-02	-5.81E-07	8.91E-02	-5.80E-07	8.91E-02
0.58125	7.29E-07	3.51E-01	7.23E-07	3.50E-01	7.23E-07	3.50E-01
0.61875	2.66E-07	-3.55E-02	2.71E-07	-3.42E-02	2.71E-07	-3.41E-02
0.65625	-5.22E-06	-6.48E-02	-5.21E-06	-6.63E-02	-5.21E-06	-6.64E-02
0.69375	2.12E-05	2.48E+00	2.12E-05	2.48E+00	2.12E-05	2.48E+00
0.73125	-6.49E-05	-8.82E+00	-6.48E-05	-8.81E+00	-6.48E-05	-8.81E+00

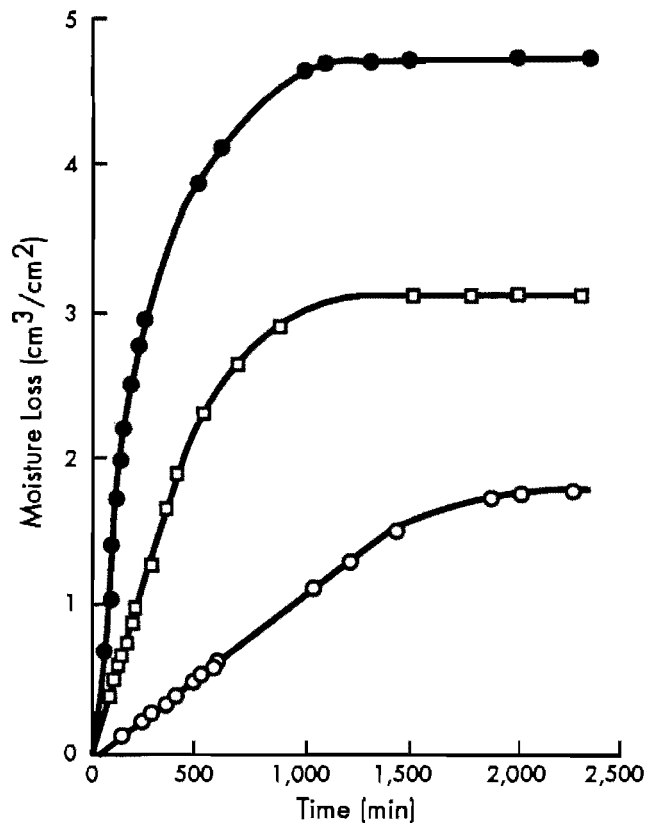


Figure 6.1 Measured fluxes of water from specimens of Taylor Marl dried at three different rates (from Kayyal, 1986)

6.4 TYPICAL RESULTS

The results of a simulation in which a specimen having Poisson's ratio of 0.33 was dried at the lowest rate of drying, 0.0019 in.³/min., are summarized in Figures 6.1 through 6.7. These results are typical of the results of simulations using different rates of drying and different Poisson's ratios. The deformation of the specimen due to drying at a constant rate can be seen in Figures 6.2 and 6.3, which show the variation of void ratios and displacements, respectively, across the radius of the specimen at different times. The void ratio and displacement are seen to vary non-linearly for any given time, with greater deformation at the surface than in the interior. For example, at 50 minutes, the surface displacement, from Figure 6.3, is already 0.02 inches, while there is little or no displacement of the specimen from the central axis to a radius of approximately 0.4 inches. Similarly for the void ratio, from Figure 6.2, at 50 minutes the void ratio of the surface of the specimen has been reduced to approximately 0.6, while the void ratio of the inner half of the specimen remains at the initial value of 0.91.

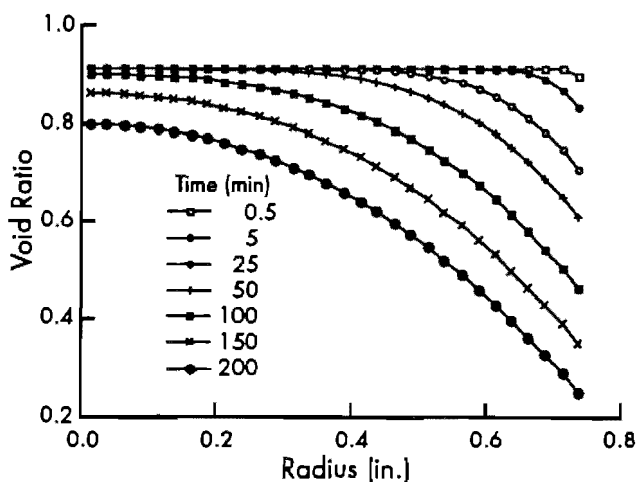


Figure 6.2 Radial distribution of void ratio at different times during drying. Rate of drying, $q = 0.0019$ cu. in./min. Poisson's ratio, $\nu = 0.33$. Bulk modulus of elasticity, $K = 1,000$ psi

The variations of radial and circumferential total stresses across the radius of the specimen are shown in Figures 6.4 and 6.5, respectively. The radial total stress is positive (compressive); the magnitude is close to zero near the surface and increases toward the central axis. As drying proceeds the magnitude of the radial total stress in the specimen increases, and after 200 minutes of drying the value at the center of the specimen is approximately 60 psi. The circumferential total stress

near the surface of the specimen is negative (tensile) and becomes more negative as drying continues. Near the central axis of the specimen the circumferential total stress is positive and becomes more positive as drying proceeds. At all times shown in Figures 6.4 and 6.5, the radial and circumferential total stresses are nearly equal near the center of the specimen.

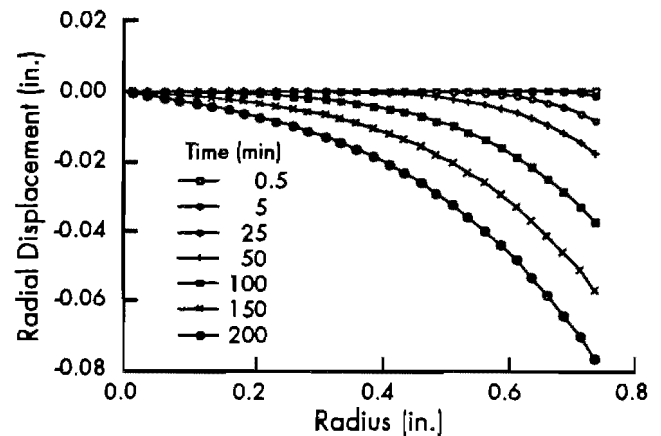


Figure 6.3 Radial distribution of radial displacement at different times during drying. Rate of drying, $q = 0.0019$ cu. in./min. Bulk modulus of elasticity, $K = 1,000$ psi. Poisson's ratio, $\nu = 0.33$

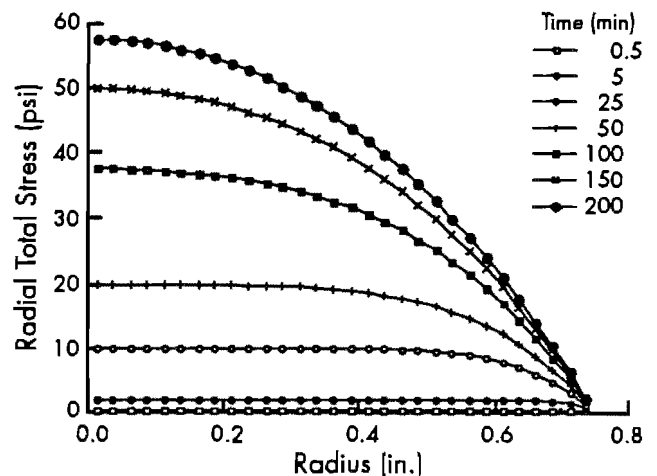


Figure 6.4 Radial distribution of radial total stress at different times during drying. Rate of drying, $q = 0.0019$ cu. in./min. Poisson's ratio, $\nu = 0.33$. Bulk modulus of elasticity, $K = 1,000$ psi

The variation of pore water pressure across the radius of the specimen is shown in Figure 6.6. The pore water pressures are seen to increase near the beginning of drying, with the largest initial increase near the surface of the specimen. The

increase in pore water pressure is called the Mandel-Cryer effect. As discussed in Chapter 5, the increase in pore water pressures is caused by the changing total stresses in the specimen. As drying continues, the pore water pressures near the surface of the specimen decrease rapidly. Near the center of the specimen the pore water pressures continue to increase well after the beginning of drying because the radial and circumferential total stresses are also increasing in this region. Eventually, the pore water pressures begin to decrease as water is removed from the interior of the specimen and the total stresses do not continue to increase significantly.

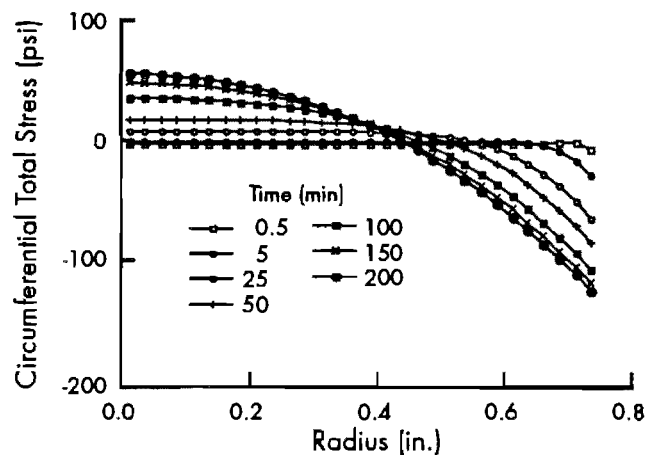


Figure 6.5 Radial distribution of circumferential total stress at different times during drying. Rate of drying, $q = 0.0019$ cu. in./min. Bulk modulus of elasticity, $K = 1000$ psi. Poisson's ratio, $\nu = 0.33$

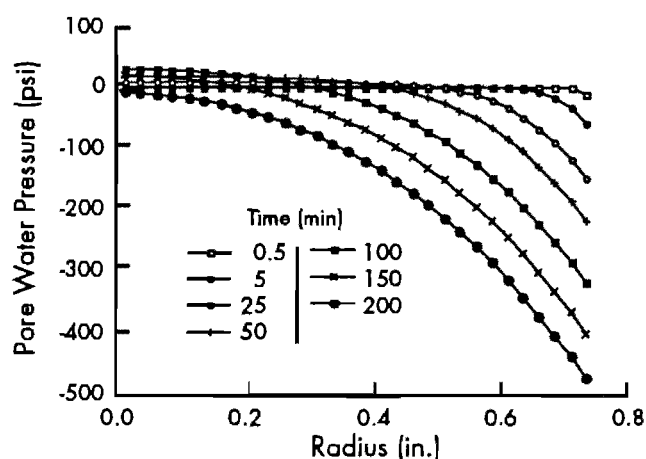


Figure 6.6 Radial distribution of pore water pressure at different times during drying. Rate of drying, $q = 0.0019$ cu. in./min. Bulk modulus of elasticity, $K = 1000$ psi. Poisson's ratio, $\nu = 0.33$

Figures 6.7 and 6.8 show the variations of radial and circumferential effective stresses, respectively, across the radius of the specimen. Near the center of the specimen, the radial effective stresses are approximately equal to the circumferential effective stresses because the pore water pressures increase at about the same rate as the total stresses. Away from the center of the specimen, the effective stresses are seen to increase significantly. Moving toward the surface of the specimen, the radial effective stress increases more rapidly than the circumferential effective stress during drying. This difference is caused by the significant difference between the radial and circumferential total stresses in this region, as discussed above. The circumferential effective stress at the surface is approximately 350 psi, and the radial effective stress at the surface is almost 500 psi after 200 minutes of drying at the lowest rate.

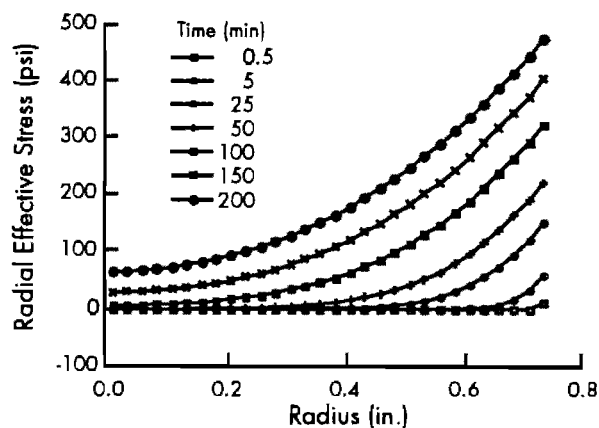


Figure 6.7 Radial distribution of radial effective stress at different times during drying. Rate of drying, $q = 0.0019$ cu. in./min. Poisson's ratio, $\nu = 0.33$. Bulk modulus of elasticity, $K = 1000$ psi

6.5 INTERPRETATION OF RESULTS

According to the equation of equilibrium of a soil element presented in Chapter 3 (Equation 3.4), the radial and circumferential total stresses are related by:

$$\frac{\partial \sigma_r}{\partial r} + \frac{\sigma_r - \sigma_\theta}{r} = 0 \quad 6.1$$

where σ indicates total stress and subscripts "r" and "θ" indicate the radial and circumferential directions, respectively. An examination of Figure 6.4 reveals that near the central axis of the specimen the radial total stress is constant across much of the specimen at early times; therefore the rate of

change of radial total stress $\left(\frac{\partial \bar{\sigma}_r}{\partial r}\right)$ is zero. According to Equation 6.1, the radial and circumferential total stresses will then be equal. This is consistent with the observation made in Section 6.4. Applying Terzaghi's principle of effective stress, Equation 6.1 can be rewritten as:

$$r \frac{\partial \bar{\sigma}_r}{\partial r} + r \frac{\partial p}{\partial r} = \bar{\sigma}_\theta - \bar{\sigma}_r \tag{6.2}$$

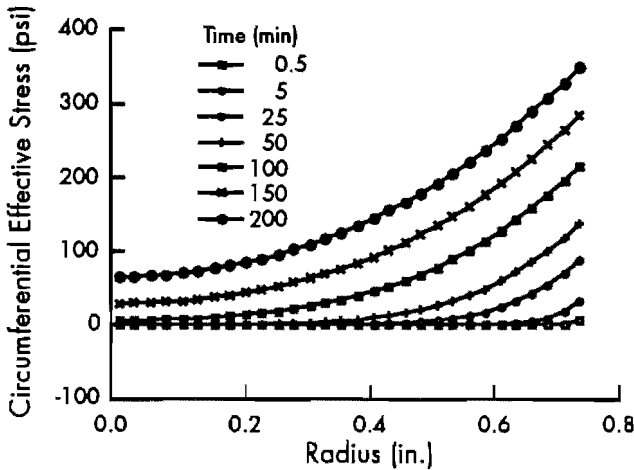


Figure 6.8 Radial distribution of circumferential effective stress at different times during drying. Rate of drying, $q = 0.0019$ cu. in./min. Poisson's ratio, $\nu = 0.33$. Bulk modulus of elasticity, $K = 1,000$ psi

Examining Figures 6.4 and 6.5 and comparing the magnitudes of the rates of change of radial effective stress and pore water pressure with respect to the radial direction near the surface of the specimen indicates:

$$\frac{\partial p}{\partial r} < 0 \tag{6.3}$$

$$\frac{\partial \bar{\sigma}_r}{\partial r} > 0 \tag{6.4}$$

and

$$\left| \frac{\partial p}{\partial r} \right| > \left| \frac{\partial \bar{\sigma}_r}{\partial r} \right| \tag{6.5}$$

Thus, the quantity on the left-hand side of Equation 6.2 is less than zero. Thus:

$$\bar{\sigma}_\theta - \bar{\sigma}_r < 0$$

This is also consistent with the observation that the radial effective stress is greater than the circumferential effective stress at the surface of the specimen.

In Section 6.4 it was noted that near the beginning of drying the pore water pressures near the surface of the specimen increase due to an increase in total stresses in the specimen. At these early times the radial effective stress is not very large. It is possible for the rate of change of pore

water pressure in the radial direction $\left(\frac{\partial p}{\partial r}\right)$ at the

surface of the specimen to be sufficiently large such that the circumferential effective stress becomes negative. If the circumferential effective stress is highly negative (tensile), it may exceed the tensile strength of the soil and cause the soil to crack at the surface.

6.6 EFFECT OF RATE OF DRYING

Kayyal (1986) has noted that laboratory specimens dried at a high rate were subject to surface cracking, while specimens dried slowly were not subject to cracking. To examine the effect of different rates of drying, a series of computations was performed using rates of drying of 0.0019 in.³/min., 0.0057 in.³/min., and 0.0280 in.³/min. and a specimen with characteristics described in Section 6.3. Poisson's ratio was assumed to be 0.33. The effect of the rate of drying on the circumferential effective stress is shown in Figures 6.9 and 6.10 for a time of 0.5 minutes, and in Figure 6.11 for a time of 2.5 minutes. Figure 6.9 shows the variation of the circumferential effective stress across the entire radius of the specimen at 0.5 minutes. It can be seen that near the beginning of drying the only changes in effective stresses occur in the specimen between a radius of 0.6 inches to 0.75 inches. Figure 6.10 shows an enhanced view of this near-surface zone of the specimen in order to focus on the changes in stresses caused by drying. All remaining figures in this chapter will be presented in this form.

As shown in Figure 6.10, for the highest rate of drying, a zone of significant tensile stress, approximately 0.05 inches wide, exists near the surface after 0.5 minutes of drying. The largest tensile stress in this zone is approximately 4 psi. A very small tensile stress exists for drying at the medium rate, and no tensile stress exists for drying at the lowest rate. The circumferential effective stress at the outer surface of the specimen at 0.5 minutes is

less than 10 psi at the lowest rate, approximately 17 psi at the medium rate, and almost 90 psi at the highest rate of drying.

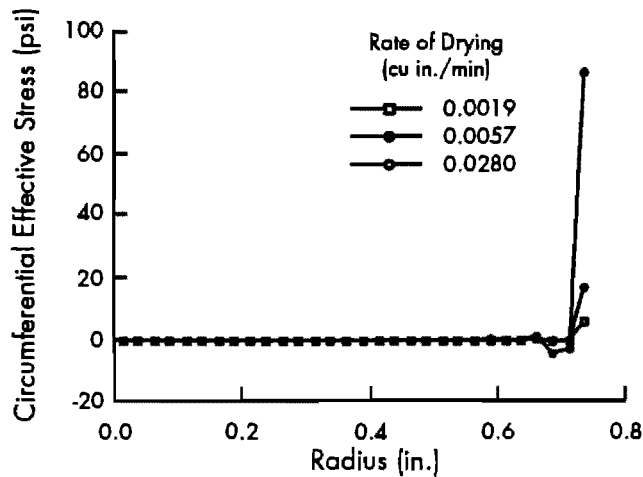


Figure 6.9 Effect of rate of drying on radial distribution of circumferential effective stress after 0.5 minutes of drying. Bulk modulus, $K = 1,000$ psi. Poisson's ratio, $\nu = 0.33$

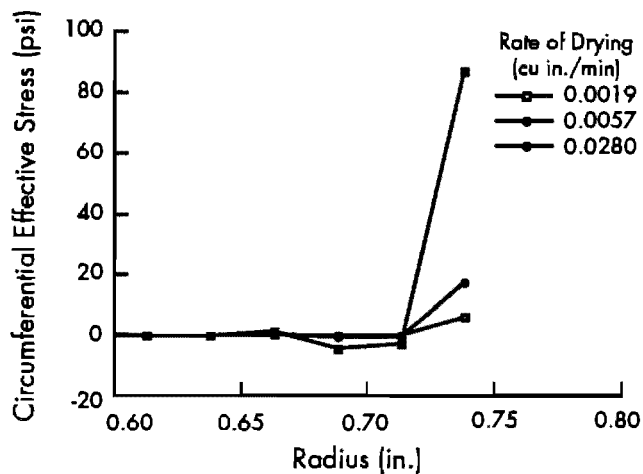


Figure 6.10 Effect of rate of drying on radial distribution of circumferential effective stress after 0.5 minutes of drying. Bulk modulus, $K = 1,000$ psi. Poisson's ratio, $\nu = 0.33$. (Enhanced view showing near-surface zone of specimen)

According to the results shown in Figure 6.11, no tensile stress exists in the soil after 2.5 minutes of drying at the two lower rates. Only a very small tensile stress can be observed for drying at the highest rate. The tensile zone appears to shift inward toward the central axis of the specimen and rapidly decrease in intensity as drying progresses. The stress at the surface increased to 20 psi for

the low rate, 57 psi for the medium rate, and almost 300 psi for the highest rate.

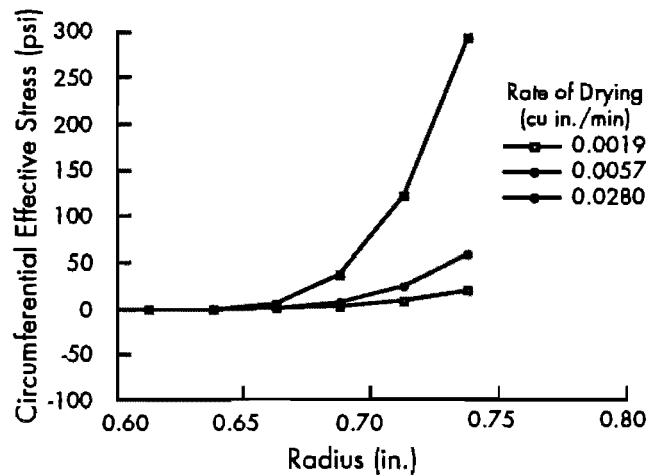


Figure 6.11 Effect of rate of drying on radial distribution of circumferential effective stress after 2.5 minutes of drying. Bulk modulus, $K = 1000$ psi. Poisson's ratio, $\nu = 0.33$. (Enhanced view showing near-surface zone of specimen)

Similar effects to those described for the circumferential stresses are evident in the radial effective stresses, as shown in Figures 6.12 and 6.13 for 0.5 minutes and 2.5 minutes of drying, respectively. After 0.5 minutes of drying at the highest rate, a zone of tensile stress approximately 0.05 inches wide exists near the surface of the specimen. The highest tensile stress in this zone is 16 psi. A much smaller tensile stress of 1 to 2 psi exists after 0.5 minutes of drying at the two lower rates. The radial stress at the surface is 12 psi for the lowest rate, 33 psi for the medium rate, and 170 psi for the highest rate of drying.

The results presented in Figure 6.13 indicate no tensile stress after 2.5 minutes of drying for any of the three rates considered. The stress at the surface at 2.5 minutes is 40 psi for the lowest rate, 115 psi for the medium rate, and 560 psi for the highest rate of drying.

Pore water pressures are shown in Figures 6.14 and 6.15 for times of 0.5 minutes and 2.5 minutes, respectively. As expected, the magnitude of suction at the surface increases significantly as the rate of drying increases. After 0.5 minutes, the soil suction at the surface of the specimen is approximately 170 psi for drying at the highest rate, 34 psi for the medium rate, and 10 psi for the lowest rate of drying. Pore water pressures are positive in the zone of the specimen where negative effective stresses exist, which is indicative of the Mandel-Cryer effect. The largest pore water

pressure at the highest rate of drying is approximately 12 psi; much smaller pore water pressures of 1 to 2 psi are caused by drying at the medium and lowest rates. These magnitudes are approximately the same as those reported for the radial effective stresses in the zone of tensile stress after 0.5 minutes of drying.

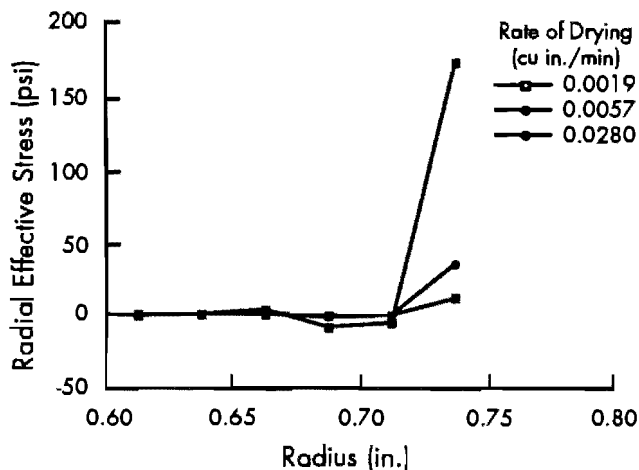


Figure 6.12 Effect of rate of drying on radial distribution of radial effective stress after 0.5 minutes of drying. Bulk modulus, $K = 1,000$ psi. Poisson's ratio, $\nu = 0.33$. (Enhanced view showing near-surface zone of specimen)

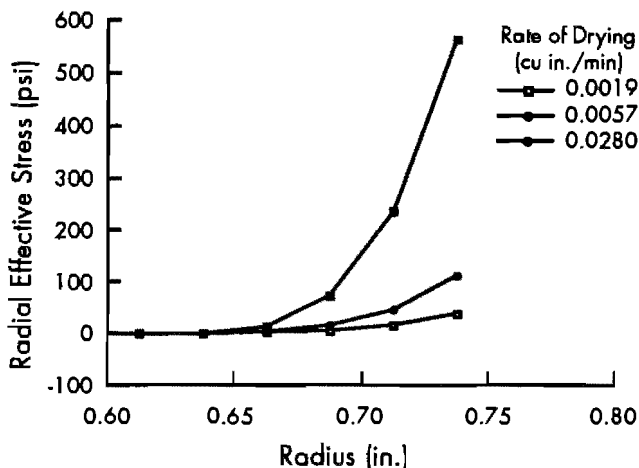


Figure 6.13 Effect of rate of drying on radial distribution of radial effective stress after 2.5 minutes of drying. Bulk modulus, $K = 1,000$ psi. Poisson's ratio, $\nu = 0.33$. (Enhanced view showing near-surface zone of specimen)

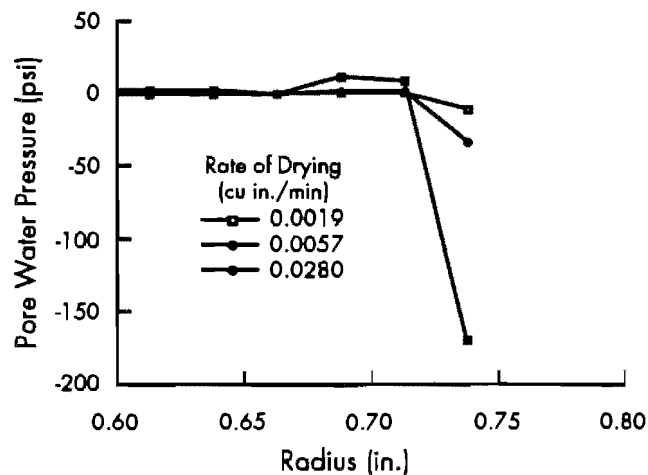


Figure 6.14 Effect of rate of drying on radial distribution of pore water pressure after 0.5 minutes of drying. Bulk modulus, $K = 1,000$ psi. Poisson's ratio, $\nu = 0.33$. (Enhanced view showing near-surface zone of specimen)

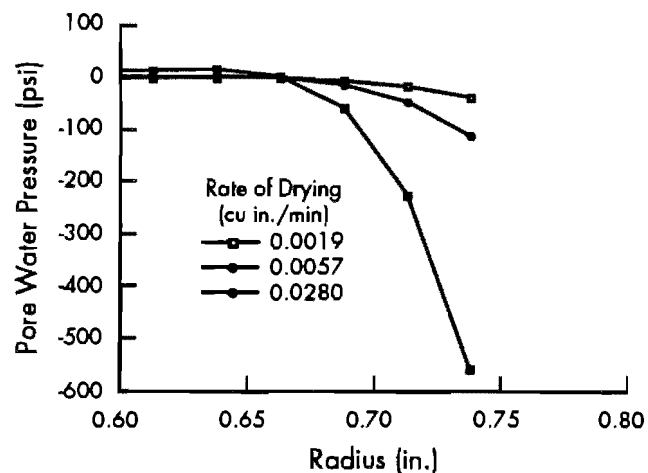


Figure 6.15 Effect of rate of drying on radial distribution of pore water pressure after 2.5 minutes of drying. Bulk modulus, $K = 1,000$ psi. Poisson's ratio, $\nu = 0.33$. (Enhanced view showing near-surface zone of specimen)

After 2.5 minutes of drying, the results in Figure 6.15 show that for drying at the highest rate the positive pore water pressures have shifted inward toward the central axis and the magnitudes of pore water pressures have increased. At the same time, the pore water pressures at the outer surface of the specimen have decreased dramatically to approximately -560 psi. Pore water pressures in the

interior of the specimen have not increased significantly after 2.5 minutes of drying at lower rates. The pore water pressures at the surface of the specimen at this time are on the order of -100 psi.

The radial variations in void ratio for different rates of drying are shown in Figures 6.16 and 6.17 at 0.5 minutes and 2.5 minutes of drying, respectively. These figures indicate that the variations in void ratio for different rates of drying generally resemble the variations in pore water pressures, as discussed above. The void ratio of the surface element decreases rapidly as water is removed from the surface, and the void ratios of some interior elements actually increase slightly. After 2.5 minutes of drying at the highest rate, the void ratio at the surface has been significantly reduced, to a value below 0.2, as seen in Figure 6.17. Continued drying at this rate would create a calculated volume change of the element which is greater than the initial volume of voids in the element. Because this condition cannot exist, comparison of results at larger times is not justified and the time of 2.5 minutes was selected as the end of drying based on the criteria established in Section 6.3.

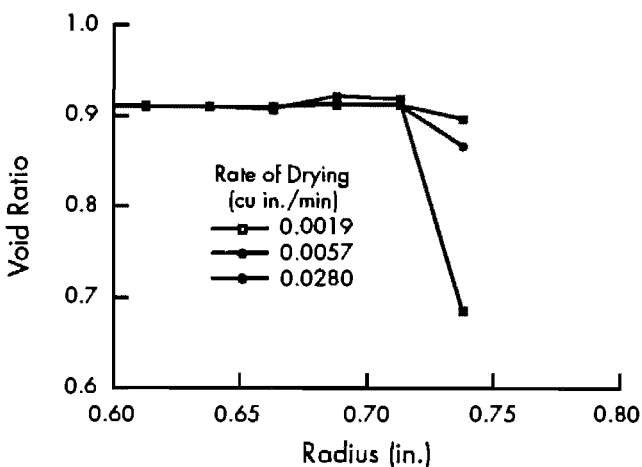


Figure 6.16 Effect of rate of drying on radial distribution of void ratio after 0.5 minutes of drying. Bulk modulus, $K = 1000$ psi. Poisson's ratio, $\nu = 0.33$. (Enhanced view showing near-surface zone of specimen)

6.7 EFFECT OF POISSON'S RATIO

A series of calculations to investigate the effect of Poisson's ratio on the predicted behavior of soil as it dries was performed using five different values of Poisson's ratio and the highest rate of drying, 0.0280 in.³/min. The effect of Poisson's ratio on the circumferential effective stresses in the specimen is shown in Figures 6.18 and 6.19 for 0.5

minutes and 2.5 minutes of drying, respectively. From these figures it appears that, in general, higher values of Poisson's ratio result in higher magnitudes of circumferential effective stress in the regions of compression and tension in the specimen. For Poisson's ratio of zero no circumferential stress developed. Figures 6.20 and 6.21 show the effect of Poisson's ratio on the radial effective stress at 0.5 minutes and 2.5 minutes, respectively. From these figures there is not a distinct relationship between Poisson's ratio and the radial effective stresses in the specimen.

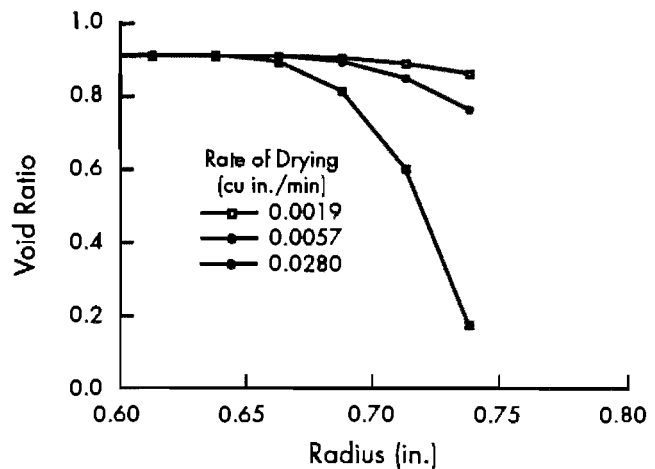


Figure 6.17 Effect of rate of drying on radial distribution of void ratio after 2.5 minutes of drying. Bulk modulus, $K = 1000$ psi. Poisson's ratio, $\nu = 0.33$. (Enhanced view showing near-surface zone of specimen)

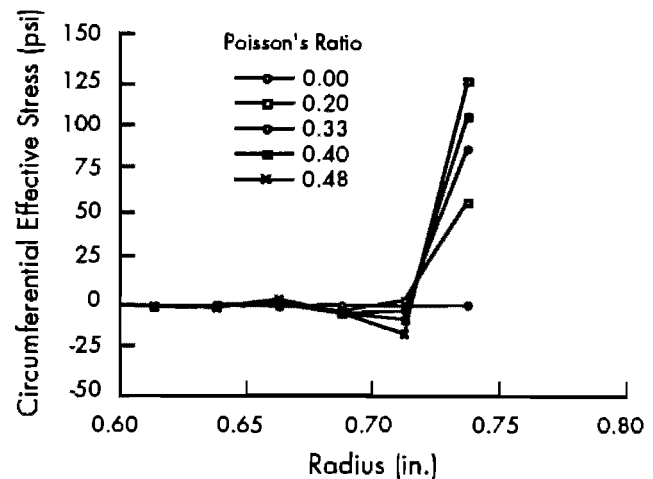


Figure 6.18 Effect of Poisson's ratio on radial distribution of circumferential effective stress after 0.5 minutes of drying at 0.0280 cu. in./min. Bulk modulus, $K = 1000$ psi. (Enhanced view showing near-surface zone of specimen)

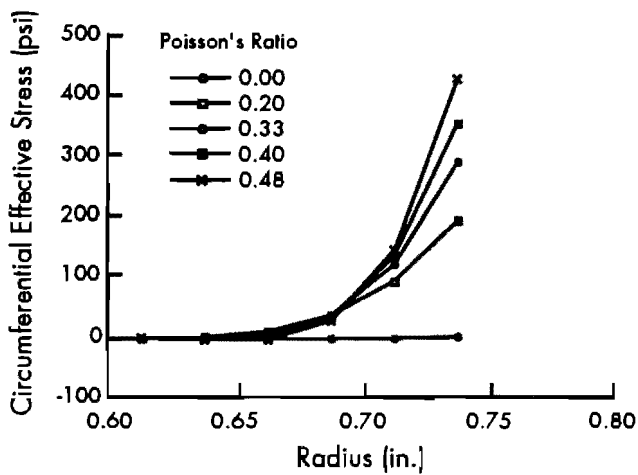


Figure 6.19 Effect of Poisson's ratio on radial distribution of circumferential effective stress after 2.5 minutes of drying at 0.0280 cu. in./min. Bulk modulus, $K = 1,000$ psi. (Enhanced view showing near-surface zone of specimen)

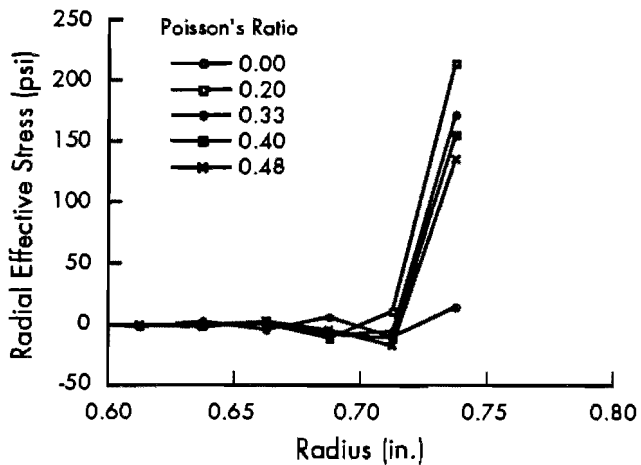


Figure 6.20 Effect of Poisson's ratio on radial distribution of radial effective stress after 0.5 minutes of drying at 0.0280 cu. in./min. Bulk modulus, $K = 1,000$ psi. (Enhanced view showing near-surface zone of specimen)

6.8 SUMMARY

The theoretical model and computer program developed in this study have been used to

investigate the effect of different rates of drying on the behavior of cylindrical specimens of Taylor clay. The results of the study indicate that higher rates of drying cause the surface of the specimen to dry more quickly than the interior of the specimen. The non-uniform drying creates a small zone of high tensile stresses near the surface of the specimen, in which both the radial and circumferential effective stresses are negative shortly after the beginning of drying. The zone of tension exists for a relatively short period of time, and, eventually, as drying continues, no tension exists in the specimen. Drying at lower rates of drying does not create a zone of significant tension at any time.

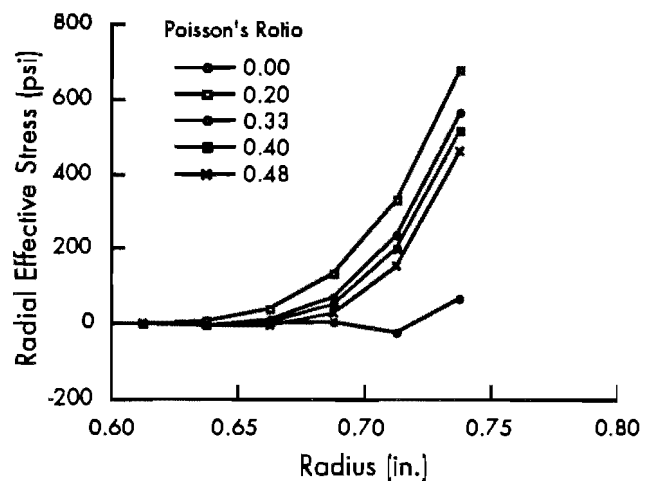


Figure 6.21 Effect of Poisson's ratio on radial distribution of radial effective stress after 2.5 minutes of drying at 0.0280 cu. in./min. Bulk modulus, $K = 1,000$ psi. (Enhanced view showing near-surface zone of specimen)

Results of the study of the effect of Poisson's ratio indicate that the magnitude of circumferential effective stress (compressive or tensile) increases as Poisson's ratio increases. For Poisson's ratio of zero there was no circumferential effective stress developed during drying. Also, a relationship between the radial effective stress and Poisson's ratio was not evident in the results.

CHAPTER 7. SUMMARY, CONCLUSIONS, AND RECOMMENDATIONS

7.1 SUMMARY

Previous research has indicated that the rate at which soil dries influences the incidence and severity of cracking in soil. A theoretical model for drying of soil based on Biot's general theory of three-dimensional consolidation was developed to investigate the effect of different rates of drying on soil behavior. The model was developed for the specific case of drying cylindrical specimens of clay of the type used in triaxial shear testing. The model assumes a homogeneous, linearly elastic soil subject only to radial flow during drying. The theoretical model consists of two coupled equations expressing the conditions of equilibrium and flow in the soil as it dries. A numerical scheme based on the finite element method was used to solve the coupled equations of the theoretical model. The numerical scheme was implemented in a computer program, called SHRINK, which was used to study the effects of different rates of drying and different values of Poisson's ratio on the behavior of Taylor Marl.

Several series of computations were performed. In the first series, five values of Poisson's ratio (0, 0.2, 0.33, 0.4, and 0.48) and a bulk modulus of elasticity of 1,000 psi were assumed. Stresses and displacements were calculated for a prescribed, sudden decrease in pore water pressure at the surface of the specimen. The relationship between the average degree of consolidation and the elapsed time was determined for each specimen and compared with results obtained using a solution based on Terzaghi's theory of consolidation. The second series of computations was also performed for five values of Poisson's ratio (0, 0.2, 0.33, 0.4, and 0.48) and a bulk modulus of elasticity of 1,000 psi. Three different rates of drying were considered: a low rate of 0.0019 in.³/min., a medium rate of 0.0057 in.³/min., and a high rate of 0.028 in.³/min. The results of computations performed at the three rates were compared for a value of Poisson's ratio of 0.33. Also, the results of the computations using the five

different values of Poisson's ratio were compared for the case of drying at a high rate.

7.2 CONCLUSIONS

The numerical model appears to realistically model the behavior of a saturated soil during drying subject to the limitations imposed by the assumption of linear elasticity. Computations with the model revealed that the total stress in the specimen changes significantly during drying. This causes an increase in the pore water pressures near the central axis of the specimen and increases the hydraulic gradient. The increase in pore water pressure is called the Mandel-Cryer effect and it accelerates the consolidation of the specimen. This causes significant differences between results obtained with the numerical model and results obtained with Terzaghi's classical theory of consolidation.

The theoretical model also shows that significantly large negative effective (tensile) stresses develop near the surface of the specimen in both the radial and, more importantly, the circumferential direction. The tensile stresses are created very early in the drying process and disappear as drying continues. The tensile stresses are created by high rates of drying, and the magnitude of the tensile stresses increases as the rate of drying increases. Low rates of drying do not create significant tensile stresses in the specimen at any time during drying. Also, the magnitudes of circumferential effective stresses (tensile and compressive) increase as Poisson's ratio increases.

The numerical model assumes that the soil is capable of withstanding the large tensile stresses created during rapid drying. In actuality, the tensile stresses are large enough to cause the soil to crack; and, once cracked, the behavior of the soil will likely be very different from that predicted by the model. However, these conclusions are consistent with the objectives of the study in that tensile stresses have been shown to develop during drying. Also, the relationship between the magnitude

of the tension and the rate of drying suggests that cracking of the soil is caused by higher rates of drying.

7.3 RECOMMENDATIONS

The numerical study of drying, reported herein, is a first attempt at understanding how soil responds to drying. The results of the numerical study indicate many potential areas for additional research. The most obvious area for further study involves modeling non-linear soil response with particular attention to increasing soil stiffness caused by drying. It would be interesting to model cracking of the soil and investigate the effect of surface cracks on the subsequent behavior of soil as it dries. The effect of combined axial and radial deformation and water flow also needs to be investigated. Other possible theoretical studies include: (1) consideration of unsaturated flow, (2) consideration of a drying front, and (3) consideration of heat transfer and non-isothermal conditions.

A rigorous treatment of the process of evaporation at the soil surface is also possible. The

equation that governs the rate of evaporation from soil, Equation 2.1, could be coupled directly to the pore water pressures at the soil surface by using Equation 2.4. The effect of variable atmospheric conditions could then be investigated by specifying a variation in concentration of water vapor in the atmosphere, which reflects the effects of changing air temperature, air pressure, or air velocity. The influence of surface roughness and variable air velocity could also be considered by specifying an appropriate variation of the mass eddy diffusivity with time.

A number of experimental investigations are needed to verify the theoretical and numerical studies. A study to determine typical rates of drying of soil under different field conditions is necessary. Given this information, it would then be possible to conduct a laboratory study of the effect of different rates of drying on the shrinkage and cracking of soil which would compare with the present study. The existence of the Mandel-Cryer effect in real soils could also be investigated in the laboratory by measuring pore water pressures during consolidation.

This page replaces an intentionally blank page in the original.

-- CTR Library Digitization Team

APPENDIX A

A.1 INTRODUCTION

The two coupled equations of equilibrium and flow developed in Chapter 4 contain vectors \mathbf{U} and \mathbf{P} , the unknowns for which the equations are solved and “stiffness” matrices \mathbf{K} , \mathbf{A} , \mathbf{C} , and \mathbf{F} , which are banded matrices whose values are determined by combining the soil properties and the element shape functions, according to the expressions presented in Chapter 4. Because each of these four matrices is composed of different combinations of the same shape functions it is possible to expand the integrals and reduce each of the expressions for the stiffness matrices to a combination of five basic matrices which have been called “component” matrices. The following pages provide a detailed derivation of the final expressions for the stiffness matrices in terms of the component matrices. Analytical expressions which can be used to exactly evaluate the component matrices are also provided.

A.2 EQUILIBRIUM EQUATION

Recall from Chapter 4 the matrix equation expressing the equilibrium of an individual element:

$$\mathbf{K}^{(e)}\mathbf{U}^{(e)} = -\mathbf{A}^{(e)}\mathbf{P}^{(e)} + \mathbf{R}^{(e)}$$

where

$$\mathbf{K}^{(e)} = \int_{r_1}^{r_2} \mathbf{B}^T \mathbf{D} \mathbf{B} r dr$$

$$\mathbf{A}^{(e)} = \int_{r_1}^{r_2} \mathbf{B}^T \mathbf{m} \mathbf{N}^T r dr$$

The vector containing the equivalent nodal forces, $\mathbf{R}^{(e)}$, is unknown for each element; but, as discussed in Chapter 4, it is not necessary to evaluate this vector because it will be removed from the solution upon assembly of the global matrix equations. Therefore, the $\mathbf{R}^{(e)}$ vector will not be considered in the following derivation.

Recall that:

$$\mathbf{N}^T = [N_1 N_2] = \begin{bmatrix} \frac{r_2 - r}{r_2 - r_1} & \frac{r - r_1}{r_2 - r_1} \end{bmatrix}$$

$$\mathbf{B} = \begin{bmatrix} -\frac{\partial N_1}{\partial r} & -\frac{\partial N_2}{\partial r} \\ \frac{N_1}{r} & \frac{N_2}{r} \end{bmatrix} = \begin{bmatrix} \frac{1}{r_2 - r_1} & \frac{-1}{r_2 - r_1} \\ -\frac{r_2 - r}{r(r_2 - r_1)} & \frac{r - r_2}{r(r_2 - r_1)} \end{bmatrix}$$

$$\mathbf{m} = \begin{bmatrix} 1 \\ 1 \end{bmatrix}$$

and

$$\mathbf{D} = \frac{E}{(1-2\nu)(1+\nu)} \begin{bmatrix} 1-\nu & \nu \\ \nu & 1-\nu \end{bmatrix}$$

Consider matrix $\mathbf{K}^{(e)}$:

$$\begin{aligned} \mathbf{B}^T \mathbf{D} \mathbf{B} &= \frac{E}{(1-2\nu)(1+\nu)} \begin{bmatrix} -N'_1 & -\frac{N_1}{r} \\ -N'_2 & -\frac{N_2}{r} \end{bmatrix} \begin{bmatrix} 1-\nu & \nu \\ \nu & 1-\nu \end{bmatrix} \begin{bmatrix} -N'_1 & -N'_2 \\ -\frac{N_1}{r} & -\frac{N_2}{r} \end{bmatrix} \\ &= \frac{E}{(1-2\nu)(1+\nu)} \begin{bmatrix} (1-\nu)N'_1N'_1 + \frac{(1-\nu)}{r^2}N_1N_1 & (1-\nu)N'_1N'_2 + \frac{(1-\nu)}{r^2}N_1N_2 \\ + \frac{2\nu}{r}N'_1N_1 & + \frac{\nu}{r}(N'_1N_2 + N_1N'_2) \\ (1-\nu)N'_1N'_2 + \frac{(1-\nu)}{r^2}N_1N_2 & (1-\nu)N'_2N'_2 + \frac{(1-\nu)}{r^2}N_2N_2 \\ + \frac{\nu}{r}(N'_1N_2 + N_1N'_2) & + \frac{2\nu}{r}N'_2N_2 \end{bmatrix} \\ &= \frac{(1-\nu)E}{(1-2\nu)(1+\nu)} \begin{bmatrix} N'_1N'_1 + \frac{1}{r^2}N_1N_1 & N'_1N'_2 + \frac{1}{r^2}N_1N_2 \\ N'_1N'_2 + \frac{1}{r^2}N_1N_2 & N'_2N'_2 + \frac{1}{r^2}N_2N_2 \end{bmatrix} \\ &\quad + \frac{\nu E}{(1-2\nu)(1+\nu)} \begin{bmatrix} \frac{2}{r}N'_1N_1 & \frac{1}{r}(N'_1N_2 + N_1N'_2) \\ \frac{1}{r}(N'_1N_2 + N_1N'_2) & \frac{2}{r}N'_2N_2 \end{bmatrix} \end{aligned}$$

Let $\lambda = \frac{\nu E}{(1-2\nu)(1+\nu)}$. Then $\lambda + 2G = \frac{(1-\nu)E}{(1-2\nu)(1+\nu)}$.

Then:

$$\begin{aligned} \mathbf{B}^T \mathbf{D} \mathbf{B} &= (\lambda + 2G) \begin{bmatrix} N'_1N'_1 & N'_1N'_2 \\ N'_1N'_2 & N'_2N'_2 \end{bmatrix} + (\lambda + 2G) \begin{bmatrix} \frac{1}{r^2}N_1N_1 & \frac{1}{r^2}N_1N_2 \\ \frac{1}{r^2}N_1N_2 & \frac{1}{r^2}N_2N_2 \end{bmatrix} \\ &\quad + \lambda \begin{bmatrix} \frac{2}{r}N'_1N_1 & \frac{1}{r}(N'_1N_2 + N_1N'_2) \\ \frac{1}{r}(N'_1N_2 + N_1N'_2) & \frac{2}{r}N'_2N_2 \end{bmatrix} = (\lambda + 2G) \mathbf{A1}^* + (\lambda + 2G) \mathbf{A2}^* + \lambda \mathbf{A3}^* \end{aligned}$$

And

$$\mathbf{K} = (\lambda + 2G) \int_{r_1}^{r_2} \mathbf{A1}^* r dr \quad + \quad (\lambda + 2G) \int_{r_1}^{r_2} \mathbf{A2}^* r dr \quad + \quad \lambda \int_{r_1}^{r_2} \mathbf{A3}^* r dr$$

or

$$\mathbf{K}^{(e)} = (\lambda + 2G)[\mathbf{A1} + \mathbf{A2}] + \lambda[\mathbf{A3} + \mathbf{A3}^T]$$

where

$$\mathbf{A1} = \begin{bmatrix} \int_{r_1}^{r_2} N_1' N_1' r dr & \int_{r_1}^{r_2} N_1' N_2' r dr \\ \int_{r_1}^{r_2} N_1' N_2' r dr & \int_{r_1}^{r_2} N_2' N_2' r dr \end{bmatrix}$$

$$\mathbf{A2} = \begin{bmatrix} \int_{r_1}^{r_2} \frac{1}{r} N_1 N_1 dr & \int_{r_1}^{r_2} \frac{1}{r} N_1 N_2 dr \\ \int_{r_1}^{r_2} \frac{1}{r} N_1 N_2 dr & \int_{r_1}^{r_2} \frac{1}{r} N_2 N_2 dr \end{bmatrix}$$

$$\mathbf{A3} = \begin{bmatrix} \int_{r_1}^{r_2} N_1' N_1 dr & \int_{r_1}^{r_2} N_1' N_2 dr \\ \int_{r_1}^{r_2} N_1 N_2' dr & \int_{r_1}^{r_2} N_2' N_2 dr \end{bmatrix}$$

Now consider matrix $\mathbf{A}^{(e)}$:

$$\begin{aligned} \mathbf{B}^T \mathbf{m} \mathbf{N}^T &= \begin{bmatrix} -N_1' & -\frac{N_1}{r} \\ -N_2' & -\frac{N_2}{r} \end{bmatrix} \begin{bmatrix} 1 \\ 1 \end{bmatrix} \begin{bmatrix} N_1 & N_2 \end{bmatrix} \\ &= \begin{bmatrix} -N_1' N_1 - \frac{1}{r} N_1 N_1 & -N_1' N_2 - \frac{1}{r} N_1 N_2 \\ -N_1 N_2' - \frac{1}{r} N_1 N_2 & -N_2' N_2 - \frac{1}{r} N_2 N_2 \end{bmatrix} \\ &= - \begin{bmatrix} N_1' N_1 & N_1' N_2 \\ N_1 N_2' & N_2' N_2 \end{bmatrix} - \begin{bmatrix} \frac{1}{r} N_1 N_1 & \frac{1}{r} N_1 N_2 \\ \frac{1}{r} N_1 N_2 & \frac{1}{r} N_2 N_2 \end{bmatrix} \\ &= -\mathbf{A4} - \mathbf{A5} \end{aligned}$$

So:

$$\mathbf{A}^{(e)} = \int_{r_1}^{r_2} \mathbf{B}^T \mathbf{m} \mathbf{N}^T r dr = -\mathbf{A4} - \mathbf{A5}$$

where

$$\mathbf{A4} = \begin{bmatrix} \int_{r_1}^{r_2} N_1' N_1 r dr & \int_{r_1}^{r_2} N_1' N_2 r dr \\ \int_{r_1}^{r_2} N_1 N_2' r dr & \int_{r_1}^{r_2} N_2' N_2 r dr \end{bmatrix}$$

and

$$\mathbf{A5} = \begin{bmatrix} \int_{r_1}^{r_2} N_1 N_1 \, dr & \int_{r_1}^{r_2} N_1 N_2 \, dr \\ \int_{r_1}^{r_2} N_1 N_2 \, dr & \int_{r_1}^{r_2} N_2 N_2 \, dr \end{bmatrix}$$

A.3 FLOW EQUATION

Recall from Chapter 4 the equation describing the flow of water through the soil element:

$$\mathbf{C}^{(e)} \dot{\mathbf{U}}^{(e)} + \mathbf{F}^{(e)} \mathbf{P}^{(e)} = \mathbf{Q}^{(e)}$$

where

$$\mathbf{C}^{(e)} = \int_{r_1}^{r_2} \mathbf{N} \mathbf{N}'^T \, r \, dr + \int_{r_1}^{r_2} \mathbf{N} \mathbf{N}^T \, dr$$

$$\mathbf{F}^{(e)} = \frac{k_r}{\gamma_w} \int_{r_1}^{r_2} \mathbf{N}' \mathbf{N}'^T \, r \, dr$$

Consider matrix $\mathbf{C}^{(e)}$:

$$\mathbf{N} \mathbf{N}'^T = \begin{bmatrix} N_1 \\ N_2 \end{bmatrix} \begin{bmatrix} N_1' & N_2' \end{bmatrix} = \begin{bmatrix} N_1' N_1 & N_1' N_2 \\ N_2' N_1 & N_2' N_2 \end{bmatrix} = \mathbf{A4}^*{}^T$$

$$\mathbf{N} \mathbf{N}^T = \begin{bmatrix} N_1 \\ N_2 \end{bmatrix} \begin{bmatrix} N_1 & N_2 \end{bmatrix} = \begin{bmatrix} N_1 N_1 & N_1 N_2 \\ N_1 N_2 & N_2 N_2 \end{bmatrix} = r \mathbf{A5}^*$$

So

$$\mathbf{C}^{(e)} = \int_{r_1}^{r_2} \mathbf{A4}^*{}^T \, r \, dr + \int_{r_1}^{r_2} r \mathbf{A5}^* \, dr = \mathbf{A4}^T + \mathbf{A5}$$

where $\mathbf{A4}$ and $\mathbf{A5}$ have been previously defined. Notice that $\mathbf{A5}$ is symmetric, such that $\mathbf{A5} = \mathbf{A5}^T$. Then:

$$\mathbf{C}^{(e)} = \mathbf{A4}^T + \mathbf{A5}^T = [\mathbf{A4} + \mathbf{A5}]^T = -\mathbf{A}^{(e)T}$$

Consider matrix $\mathbf{F}^{(e)}$:

$$\mathbf{N}' \mathbf{N}'^T = \begin{bmatrix} N_1' \\ N_2' \end{bmatrix} \begin{bmatrix} N_1' & N_2' \end{bmatrix} = \begin{bmatrix} N_1' N_1' & N_1' N_2' \\ N_1' N_2' & N_2' N_2' \end{bmatrix} = \mathbf{A1}^*$$

So

$$\mathbf{F}^{(e)} = \frac{k_r}{\gamma_w} \int_{r_1}^{r_2} \mathbf{A1}^* \, r \, dr = \frac{k_r}{\gamma_w} \mathbf{A1}$$

where $\mathbf{A1}$ has been previously defined.

A.4 SUMMARY

The four stiffness matrices used to describe the finite element approximations of the governing equations are combinations of five basic component matrices. In program SHRINK the global stiffness matrices are assembled directly from the various combinations of these component matrices. The values of the component matrices are determined by numerical integration using the Gauss-Legendre technique. The numerical integration is necessary to avoid undefined values which would occur in matrix **A2** during integration over the first element. This matrix contains terms involving the natural logarithm which has an infinite value at $r = 0$ (the axis of the specimen).

The closed-form expression of each of the component matrices is given below:

Let $r_2 - r_1 = \Delta r$.

$$\mathbf{A1} = \int_{r_1}^{r_2} \mathbf{N}'\mathbf{N}'^T r dr = \frac{r_2^2 - r_1^2}{2\Delta r^2} \begin{bmatrix} 1 & -1 \\ -1 & 1 \end{bmatrix}$$

$$\mathbf{A2} = \int_{r_1}^{r_2} \mathbf{N}'\mathbf{N}'^T \frac{1}{r} dr = \frac{1}{\Delta r^2} \begin{bmatrix} r_2^2 \ln \frac{r_2}{r_1} - \frac{3}{2}r_2^2 - \frac{1}{2}r_1^2 + 2r_1r_2 & \frac{1}{2}r_2^2 - \frac{1}{2}r_1^2 + r_1r_2 \ln \frac{r_1}{r_2} \\ \frac{1}{2}r_2^2 - \frac{1}{2}r_1^2 + r_1r_2 \ln \frac{r_1}{r_2} & r_1^2 \ln \frac{r_2}{r_1} + \frac{3}{2}r_1^2 + \frac{1}{2}r_2^2 - 2r_1r_2 \end{bmatrix}$$

$$\mathbf{A3} = \int_{r_1}^{r_2} \mathbf{N}\mathbf{N}'^T dr = \begin{bmatrix} -\frac{1}{2} & \frac{1}{2} \\ -\frac{1}{2} & \frac{1}{2} \end{bmatrix}$$

$$\mathbf{A4} = \int_{r_1}^{r_2} \mathbf{N}\mathbf{N}^T r dr = \frac{1}{6\Delta r^2} \begin{bmatrix} -r_2^3 - 2r_1^3 + 3r_1^2r_2 & -r_1^3 - 2r_2^3 + 3r_1r_2^2 \\ r_2^3 + 2r_1^3 - 3r_1^2r_2 & r_1^3 + 2r_2^3 - 3r_1r_2^2 \end{bmatrix}$$

$$\mathbf{A5} = \int_{r_1}^{r_2} \mathbf{N}\mathbf{N}^T dr = \frac{\Delta r}{6} \begin{bmatrix} 2 & 1 \\ 1 & 2 \end{bmatrix}$$

This page replaces an intentionally blank page in the original.

-- CTR Library Digitization Team

BIBLIOGRAPHY

1. Barron, R. A. (1948) "Consolidation of Fine-Grained Soils by Drain Wells," *Transactions of the American Society of Civil Engineers*, 113, pp. 718-754.
2. Biot, Maurice A. (1941) "General Theory of Three-Dimensional Consolidation," *Journal of Applied Physics*, 12, pp. 155-164.
3. Budyko, M. I. (1963) *Evaporation Under Natural Conditions*. Translation. Jerusalem: Israel Program for Scientific Translations.
4. Cryer, C. W. (1963) "A Comparison of the Three-Dimensional Consolidation Theories of Biot and Terzaghi," *Quarterly Journal of Mechanics and Applied Mathematics*, 16, pp. 401-412.
5. Cuenca, Fernando Augusto (1989) "Stability of Reinforced Embankments Constructed of High-Plasticity Clays," Dissertation, The University of Texas at Austin, Geotechnical Engineering Dissertation GD89-2.
6. Geankoplis, C. J. (1983) *Transport Processes: Momentum, Heat and Mass*. Boston: Allyn and Bacon, Inc.
7. Gourlay, A. W., and Wright, S. G. (1984) "Initial Laboratory Study of Shear Strength Properties of Compacted Highly Plastic Clays Used for Highway Embankment Construction in the Area of Houston, Texas," *A Report on Laboratory Testing Performed Under Interagency Contract Nos. (82-83) 2187 and (84-85) 1026*, Center for Transportation Research, The University of Texas at Austin.
8. Hall, C. W. (1979) *Dictionary of Drying*. New York: Marcel Dekker, Inc.
9. Hillel, Daniel (1982) *Introduction to Soil Physics*. New York: Academic Press.
10. Hlavác, J. (1983) *The Technology of Glass and Ceramics: An Introduction*. Amsterdam: Elsevier Scientific Publishing Company.
11. Hwang, C. T., Morgenstern, N. R., and Murray, D. W. (1971) "On Solutions of Plane Strain Consolidation Problems by Finite Element Methods," *Canadian Geotechnical Journal*, 8, pp. 109-118.
12. Johnston, J. R., and Hill, H. O. (1944) "A Study of the Shrinkage and Swelling Properties of Rendzina Soils," *Soil Science Society of America, Proceedings*, 9, pp. 24-29.
13. Kayyal, Mohamad Kasim (1986) "Effects of Wetting and Drying on Long-Term Strength of Compacted Taylor Marl Clay," Thesis, The University of Texas at Austin, Geotechnical Engineering Thesis GT86-1.
14. Key, R. B. (1972) *Drying: Principles and Practice*. Oxford: Pergamon Press.
15. Lawrence, W. G. (1972) *Ceramic Science for the Potter*. Philadelphia: Chilton Book Company.

16. Lebedev, P. D. (1961) "Heat and Mass Transfer between Moist Solids and Air," *International Journal of Heat and Mass Transfer*, 1, pp. 302-305.
17. Mandel, J. (1963) "Consolidation des Sols," *Geotechnique*, 3, pp. 287-299.
18. Meiners, A. C. (1988) "Development of an Empirical Model for the Drying of Hygroscopic and Non-Hygroscopic Materials," Thesis, The University of Texas at Austin.
19. Olson, R. E. (1989) Class notes. CE 387R.1: Consolidation and Settlement. The University of Texas at Austin.
20. Olson, R. E. (1990) Personal Communication.
21. Phelps, G. W., et al. (1982) *Rheology and Rheometry of Clay-Water Systems*. Sandersville: Cyprus Industrial Minerals Co.
22. Stauffer, P. A., and Wright, S. G. (1984) "An Examination of Earth Slope Failures in Texas," Research Report 353-3F, Center for Transportation Research, The University of Texas at Austin.
23. Worrall, W. E. (1986) *Clays and Ceramic Raw Materials, Second Edition*. London: Elsevier Applied Science Publishers.
24. Zienkiewicz, O. C., and Taylor, R. L. (1989) *The Finite Element Method, Fourth Edition. Volume 1*. London: McGraw-Hill Book Company.